

Supporting Information

for

Screening Diffusion of Small Molecules in Flexible Zeolitic Imidazolate Frameworks Using a DFT Parameterized Force Field

Ross J. Verploegh¹, Ambarish Kulkarni², Salah Eddine Boulfelfel¹,
Jonathan C. Haydak¹, Dai Tang¹, David S. Sholl^{1,*}

¹*School of Chemical & Biomolecular Engineering, Georgia Institute of Technology,
Atlanta, GA 30332-0100*

²*SUNCAT Center for Interface Science and Catalysis, Department of Chemical Engineering,
Stanford University, 450 Serra Mall, Stanford, California 94305*

***CORRESPONDING AUTHOR:** david.sholl@chbe.gatech.edu

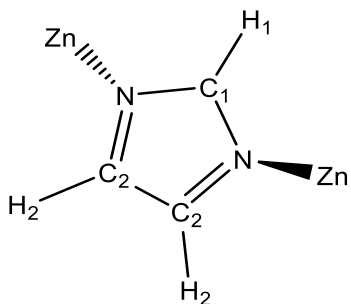
Table of Contents

Unfunctionalized Imidazolate (Im) ZIF Intramolecular Force Field Parameters.....	S3
2-Methylimidazolate (mIm) ZIF Intramolecular Force Field Parameters.....	S7
Imidazolate-2-Carboxaldehyde (ImCA) ZIF Intramolecular Force Field Parameters	S10
Benzimidazolate (BzIm) ZIF Intramolecular Force Field Parameters	S14
Modeling Zn-N-C_{1,2} and N-Zn-N Bending by Fitting to Potential Energy Scans	S17
Nonbonded Force Field Parameters for ZIFs	S19
Geometric Predictions of SALEM-2, ZIF-7, ZIF-8, ZIF-90	S24
Im and mIm ZIF Polymorphs: Geometric and Stability Predictions	S26
Born-Oppenheimer Molecular Dynamics (BOMD) Data for SALEM-2, ZIF-7, ZIF-8, and ZIF-90.....	S33
Light Gas Diffusion in SALEM-2, ZIF-8, ZIF-90, and ZIF-7	S41
Thermodynamic Stability of Im and mIm ZIF Polymorphs	S60
Supporting Information References.....	S63

Unfunctionalized Imidazolate (Im) ZIF Intramolecular Force Field Parameters

Table S.1 below contains all the intramolecular force field functions and parameters implemented for unfunctionalized ZIFs. Green (red) shaded regions indicated which degrees of freedom are (not) included in the intraZIF-FF. Comparison of spring constants between the AMBER and intraZIF FFs are also included.

Table S.1. Bonded force field parameters for ZIFs with unfunctionalized imidazolate linkers. Functional forms, spring constants, and equilibrium geometry parameters are listed.



BOND STRETCHES (6 types)

Type I-J (N*)	$k_r / \text{kcal mol}^{-1} \text{\AA}^{-2}$	$k_r / \text{kcal mol}^{-1} \text{\AA}^{-2}$	$r_{ij}^0 / \text{\AA}$
C ₁ -H ₁ (1)	373.06	367.0	1.09
C ₁ -N (2)	362.69	488.0	1.35
C ₂ -N (2)	299.01	410.0	1.38
C ₂ -H ₂ (2)	381.32	367.0	1.09
C ₂ -C ₂ (1)	389.86	518.0	1.38
Zn-N (2)	70.67 ^H	78.5 ^{A,1} , 86.0 ^{A,2}	2.00

$$\text{Morse: } U_{\text{Zn}-\text{N}} = \sum D_r (1 - e^{-\alpha(r_{ij} - r_{ij}^0)})^2$$

Type I-J (N*)	$D_r / \text{kcal mol}^{-1}$	$\alpha / \text{\AA}^{-1}$	$r_{ij}^0 / \text{\AA}$
Zn-N (2)	26.08	2.09	2.00

ANGLE BENDING (9 types)

Type I-J-K (N*)	$k_\theta / \text{kcal mol}^{-1} \text{rad}^{-2}$	$k_\theta / \text{kcal mol}^{-1} \text{rad}^{-2}$	$\theta_{ijk}^0 / {}^\circ \text{degrees}$
C ₂ -C ₂ -H ₂ (2)	65.15	50.0	130.66
N-C ₁ -N (1)	104.91	70.0	112.49

Table S.1 (continued)

N-C ₂ -C ₂ (2)	121.85	70.0	108.18
N-C ₂ -H ₂ (2)	63.42	50.0	121.16
C ₁ -N-C ₂ (2)	105.54	70.0	105.58
H ₁ -C ₁ -N (2)	52.84	50.0	123.75
C ₁ -N-Zn (2)	38.65 ^H /18.28 ^P	50.0 ^A	127.25
C ₂ -N-Zn (2)	39.84 ^H /18.84 ^P	35.0 ^A	127.17
N-Zn-N (3)	33.39 ^H /18.20 ^P	10.5 ^A	109.43

DIHEDRAL ANGLES (13 types)

Type I-J-K-L (N*)	Cosine: $U_{proper} = \sum k_\phi [1 + \cos(m_\phi \phi_{ijkl} - \phi_{ijkl}^0)]$			m / -
	k _φ / kcal mol ⁻¹	k _φ / kcal mol ⁻¹	φ _{ijkl} ⁰ / ° degrees	
N-C ₁ -N-C ₂ (2)	3.97±0.56	4.80	180.0	2
H ₁ -C ₁ -N-C ₂ (2)	3.61±0.98	4.80	180.0	2
C ₂ -C ₂ -N-C ₁ (2)	2.72±1.24	4.80	180.0	2
H ₂ -C ₂ -N-C ₁ (2)	3.43±0.75	4.80	180.0	2
N-C ₂ -C ₂ -H ₂ (2)	2.61±0.71	4.00	180.0	2
N-C ₂ -C ₂ -N (1)	1.85±1.74	4.00	180.0	2
H ₂ -C ₂ -C ₂ -H ₂ (1)	0.00	4.00	180.0	2
H ₁ -C ₁ -N-Zn (2)	0.00	NA	180.0	2
H ₂ -C ₂ -N-Zn (2)	0.00	NA	180.0	2
N-C ₁ -N-Zn (2)	0.00	NA	180.0	2
C ₂ -C ₂ -N-Zn (2)	0.00	NA	180.0	2

$$\text{Fourier series: } U_{proper} = \sum \sum_{n=1}^6 k_{\phi,n} [1 + \cos(m_n \phi_{ijkl} - d_n)]$$

Type I-J-K-L (N*)	k _φ / kcal mol ⁻¹	d _n / ° degrees	m / -
C ₁ -N-Zn-N (6)	3.02±1.48, 2.26±1.42, 0.08±0.05	0.0, 180.0, 0.0	1, 2, 3
C ₂ -N-Zn-N (6)	3.39±0.74, 1.92±0.79, 0.02±0.02	0.0, 0.0, 0.0	1, 2, 3

IMPROPER ANGLES (3 types)

Type I-J-K-L (N*)	Cosine: $U_{improper} = \sum k_\xi [1 + \cos(m_\xi \zeta_{ijkl} - \zeta_{ijkl}^0)]$			m / -
	k _ξ / kcal mol ⁻¹	k _ξ / kcal mol ⁻¹	ζ _{ijkl} ⁰ / ° degrees	
N-H ₂ -C ₂ ^P -C ₂ (2)	0.00	1.1	180.0	2
H ₁ -N-C ₁ ^P -N (1)	0.00	1.1	180.0	2
C ₁ -C ₂ -N ^P -Zn (2)	0.00	0.00	180.0	2

Improper term I-J-K-L refers to the angle between planes I-J-K and J-K-L, with J-K axis of rotation and K being the central/primary atom (noted by subscript ^P); N* = number of bonds, angles, or dihedrals in the linker-metal complex. Superscripts H, P, and A refer to Hessian matrix, potential energy scan, or AMBER in reference to where certain spring constants were obtained.

Figures S.1a, S.2a, and S.3a show the single point potential energy scans for the Zn-N bond, the N-Zn-C_{1,2} angles, and the N-Zn-N angle along with harmonic and Morse potential fits. **Figures S.1b, S.2b, and S.3b** show the contribution of the electrostatic energy for “fixed” and “varying”

charges. “Fixed charges” refer to using only one set of charges as derived from the DDEC3³⁻⁴ method on the minimum energy cluster. “Varying charges” refer to the recalculation of charges for each snapshot along the scan using the DDEC3 method. **Figure S.4** shows the low energy region of the BOMD simulations on the Im cluster.

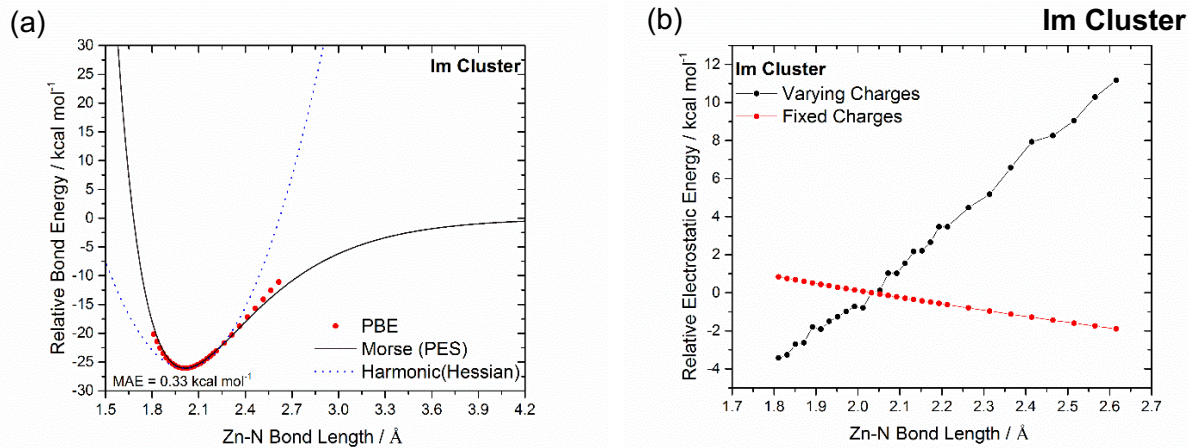


Figure S.1. **(a)** Morse potentials fit (solid black line) to potential energy scans (red dots) along the Zn-N bond. The harmonic potential with the spring constant from the Seminario method is shown for comparison (dashed blue line). The mean absolute error (MAE) of the Morse fit is also reported. **(b)** Relative coulombic energy for the Zn-N potential energy scans.

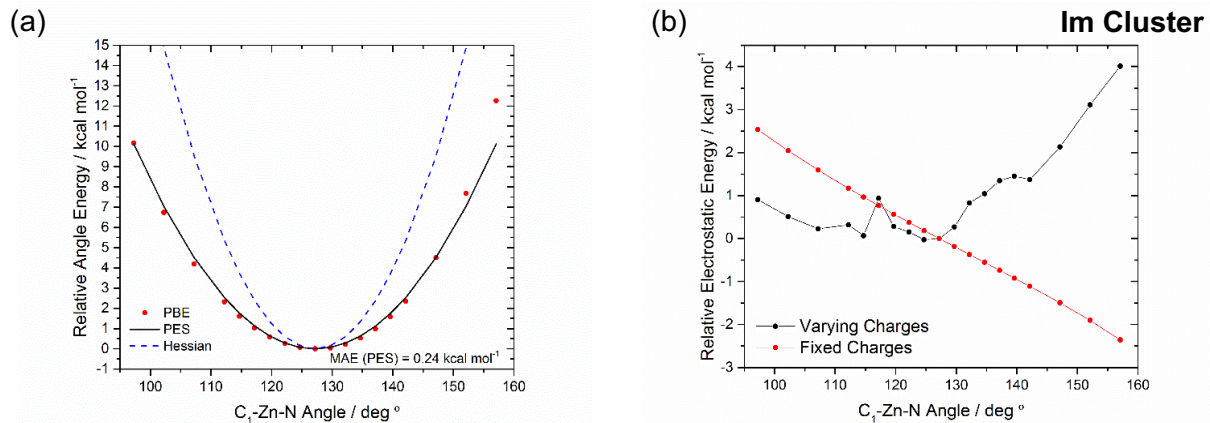


Figure S.2. Harmonic angle potential fit using the spring constant from the Seminario method (dashed blue line) and the direct PES fit (solid black line) to PES scans (red dots) of the $C_{1,2}\text{-Zn-N}$ angles. The mean absolute error of the PES fit is also reported. **(b)** Relative coulombic energy for the $C_{1,2}\text{-Zn-N}$ potential energy scans.

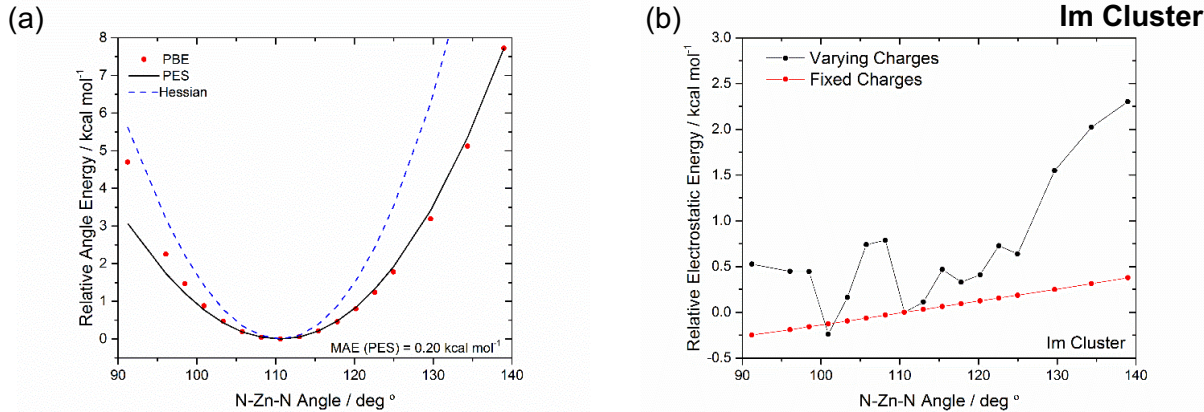


Figure S.3. **(a)** Harmonic angle potential fit using the spring constant from the Seminario method (dashed blue line) and the direct PES fit (solid black line) to PES scans (red dots) of the N-Zn-N angles. The mean absolute error of the PES fit is also reported. **(b)** Relative coulombic energy for the N-Zn-N potential energy scans.

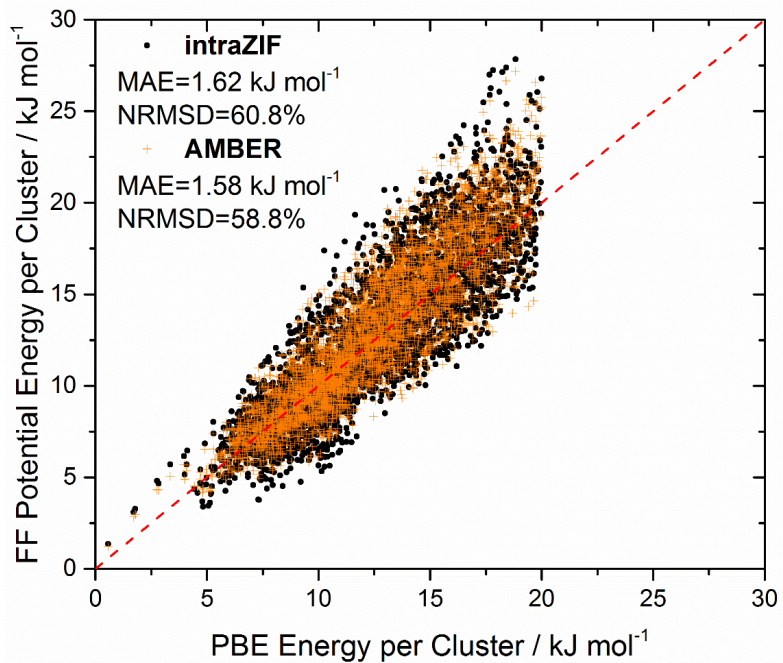
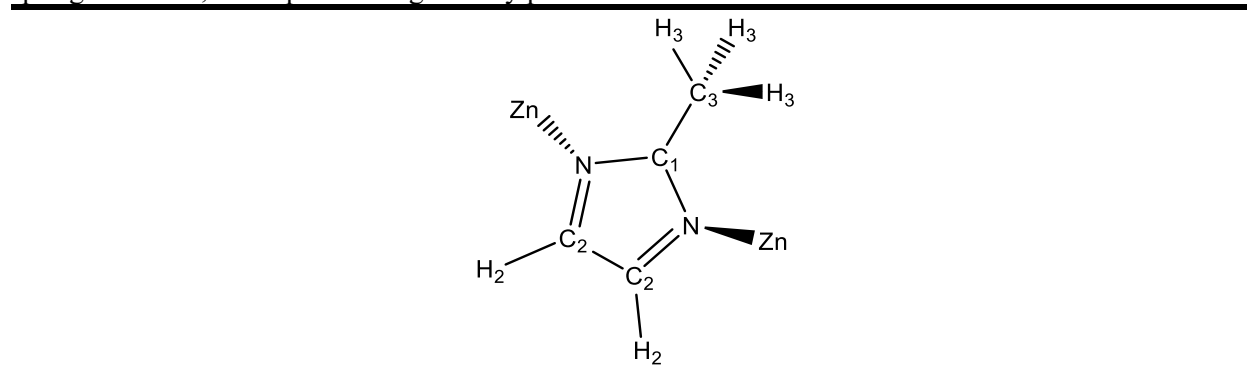


Figure S.4. Relative energy comparisons between PBE and **(a)** the intraZIF-FF (black circles) including Fourier dihedrals from the potential energy fitting as well as **(b)** the AMBER-FF (orange crosses) for the low energy region (<20 kJ mol⁻¹).

2-Methylimidazolate (mIm) ZIF Intramolecular Force Field Parameters

Table S.2 below contains all the intramolecular force field functions and parameters implemented for ZIFs with 2-methylimidazolate linkers. Green (red) shaded regions indicated which degrees of freedom are (not) included in the intraZIF-FF. Comparison of spring constants between the AMBER and intraZIF FFs are also included.

Table S.2. Bonded force field parameters for ZIFs with 2-methylimidazolate linkers. Functional forms, spring constants, and equilibrium geometry parameters are listed.



BOND STRETCHES (7 types)

Type I-J (N*)	Harmonic: $U_{stretching} = \sum_{\text{intraZIF}} k_r (r_{ij} - r_{ij}^0)^2$	AMBER	
C ₃ -H ₃ (3)	332.52	340.0	1.10
C ₁ -C ₃ (1)	248.76	346.543/317.0	1.49
C ₁ -N (2)	336.56	488.0/535.55	1.35
C ₂ -N (2)	298.63	410.0/440.21	1.38
C ₂ -H ₂ (2)	380.11	367.0	1.09
C ₂ -C ₂ (1)	402.91	540.249/518.0	1.38
Zn-N (2)	67.16 ^H	78.5 ^{A,1} , 86.0 ^{A,2}	1.99

$$\text{Morse: } U_{Zn-N} = \sum D_r (1 - e^{-\alpha(r_{ij} - r_{ij}^0)})^2$$

Type I-J (N*)	$D_r / \text{kcal mol}^{-1}$	$\alpha / \text{\AA}^{-1}$	$r_{ij}^0 / \text{\AA}$
Zn-N (2)	27.13	2.01	1.99

ANGLE BENDING (11 types)

Type I-J-K (N*)	Harmonic: $U_{bend} = \sum_{\text{intraZIF}} k_\theta (\theta_{ijk} - \theta_{ijk}^0)^2$	AMBER	
H ₃ -C ₃ -H ₃ (3)	35.88	35.0	107.95
H ₃ -C ₃ -C ₁ (3)	54.59	50.0	110.95

Table S.2 (continued)

H ₂ -C ₂ -C ₂ (2)	64.14	50.0	130.95
H ₂ -C ₂ -N (2)	63.06	50.0	121.23
C ₂ -N-C ₁ (2)	112.17	70.0	106.27
C ₂ -C ₂ -N (2)	117.58	70.0	108.04
N-C ₁ -N (1)	111.76	70.0	111.38
N-C ₁ -C ₃ (2)	106.35	70.0	124.28
Zn-N-C ₁ (2)	44.58 ^H /18.28 ^P	50.0	126.91
Zn-N-C ₂ (2)	44.45 ^H /18.84 ^P	35.0	126.81
N-Zn-N (3)	36.62 ^H /18.20 ^P	10.5	109.45

DIHEDRAL ANGLES (14 types)

Type I-J-K-L (N*)	Cosine: $U_{proper} = \sum k_\phi [1 + \cos(m \phi_{ijkl} - \phi_{ijkl}^0)]$		$\phi_{ijkl}^0 / {}^\circ$ degrees	m / -
	intraZIF	AMBER		
C ₃ -C ₁ -N-C ₂ (2)	1.48	4.15	180.0	2
N-C ₁ -N-C ₂ (2)	3.97	4.80	180.0	2
C ₂ -C ₂ -N-C ₁ (2)	2.72	4.80	180.0	2
H ₂ -C ₂ -N-C ₁ (2)	3.43	4.80	180.0	2
N-C ₂ -C ₂ -H ₂ (2)	2.61	4.00	180.0	2
N-C ₂ -C ₂ -N (1)	1.85	4.00	180.0	2
H ₂ -C ₂ -C ₂ -H ₂ (1)	0.00	4.00	180.0	2
N-C ₁ -C ₃ -H ₃ (6)	0.00	NA (<i>free rotation of methyl-group</i>)	180.0	2
C ₃ -C ₁ -N-Zn (2)	0.00	NA	180.0	2
N-C ₁ -N-Zn (2)	0.00	NA	180.0	2
C ₂ -C ₂ -N-Zn (2)	0.00	NA	180.0	2
H ₂ -C ₂ -N-Zn (2)	0.00	NA	180.0	2

$$\text{Fourier series: } U_{proper} = \sum_{n=1}^6 k_{\phi,n} [1 + \cos(m_n \phi_{ijkl} - d_n)]$$

Type I-J-K-L (N*)	$k_\phi / \text{kcal mol}^{-1}$	$d_n / {}^\circ$ degrees	m / -
C ₁ -N-Zn-N (6)	3.02±1.48, 2.26±1.42, 0.08±0.05	0.0, 180.0, 0.0	1, 2, 3
C ₂ -N-Zn-N (6)	3.39±0.74, 1.92±0.79, 0.02±0.02	0.0, 0.0, 0.0	1, 2, 3

IMPROPER ANGLES (3 types)

Type I-J-K-L (N*)	Fourier series: $U_{improper} = \sum k_\xi [1 + \cos(m \xi_{ijkl} - \xi_{ijkl}^0)]$		$\xi_{ijkl}^0 / {}^\circ$ degrees	m / -
	intraZIF	AMBER		
N-H ₂ -C ₂ ^P -C ₂ (2)	0.00	1.1	180.0	2
C ₃ -N-C ₁ ^P -N (1)	0.00	1.1	180.0	2
C ₁ -C ₂ -N ^P -Zn (2)	0.00	NA	180.0	2

Improper term I-J-K-L refers to the angle between planes I-J-K and J-K-L, with J-K axis of rotation and K being the central/primary atom (noted by subscript ^P); N*=number of bonds, angles, or dihedrals in the linker-metal complex. Superscripts H, P, and A refer to Hessian matrix, potential energy scan, or AMBER in reference to where certain spring constants were obtained.

Figure S.5a shows the single point potential energy scans for the Zn-N bond along with harmonic and Morse potential fits. **Figure S.5b** shows the contribution of the electrostatic energy for “fixed” and “varying” charges. **Figure S.6** shows the comparison of the **(a)** intraZIF-FF and **(b)** AMBER-FF predicted configurational potential energies from BOMD simulations on the cluster.

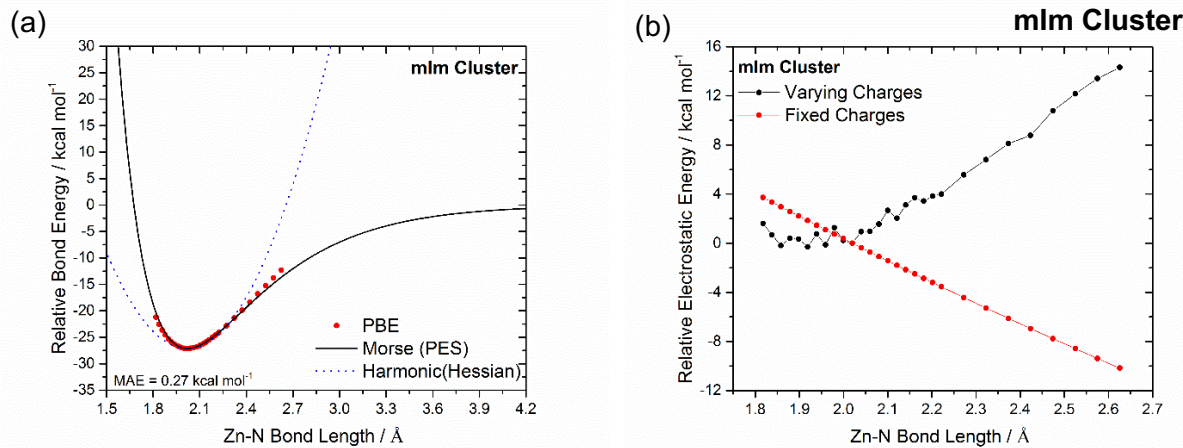


Figure S.5. **(a)** Morse potentials fit (solid black line) to potential energy scans (red dots) along the Zn-N bond. The harmonic potential with the spring constant from the Seminario method is shown for comparison (dashed blue line). The mean absolute error (MAE) of the Morse fit is also reported. **(b)** Relative coulombic energy for the Zn-N potential energy scans.

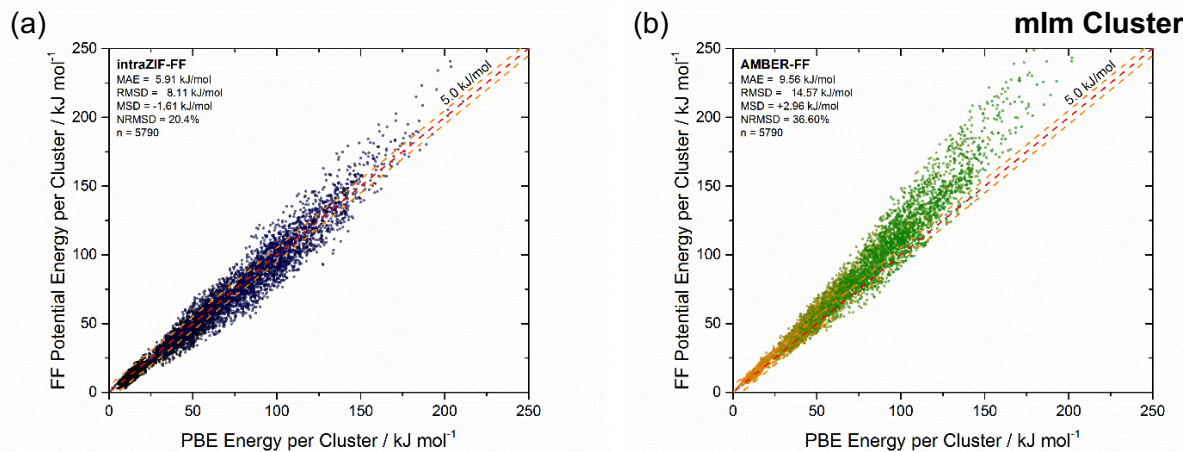


Figure S.6. Relative energy comparisons between PBE and **(a)** the intraZIF-FF including Fourier dihedrals from the potential energy fitting and **(b)** the AMBER-FF using standard cosine proper dihedrals. The color code (black to blue/intraZIF and orange to green/AMBER) is designed to easily identify the low and high energy regions.

Imidazolate-2-Carboxaldehyde (ImCA) ZIF Intramolecular Force Field Parameters

Table S.3 below contains all the intramolecular force field functions and parameters implemented for ZIFs with imidazolate-2-carboxaldehyde linkers. Green (red) shaded regions indicated which degrees of freedom are (not) included in the intraZIF-FF. Comparison of spring constants between the AMBER and intraZIF FFs are also included.

Table S.3. Bonded force field parameters for ZIFs with imidazolate-2-carboxaldehyde linkers. Functional forms, spring constants, and equilibrium geometry parameters are listed.

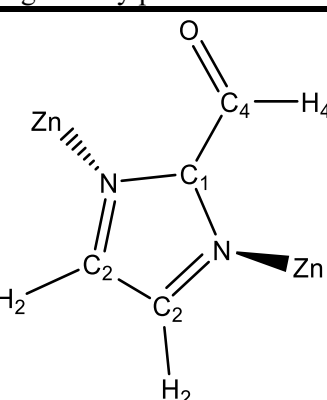
			
BOND STRETCHES (8 types)			
Type I-J (N^*)	Harmonic: $U_{stretching} = \sum_{intraZIF} k_r (r_{ij} - r_{ij}^0)^2$	AMBER	
	$k_r / kcal mol^{-1} \text{\AA}^{-2}$	$k_r / kcal mol^{-1} \text{\AA}^{-2}$	$r_{ij}^0 / \text{\AA}$
C ₄ -O (1)	692.30	570.0	1.23
C ₄ -H ₄ (1)	293.42	367.0	1.12
C ₁ -C ₄ (1)	254.22	357.2	1.45
C ₁ -N (2)	312.81	488.0	1.36
N-C ₂ (2)	348.16	410.0	1.36
C ₂ -H ₂ (2)	384.32	367.0	1.09
C ₂ -C ₂ (1)	353.87	518.0	1.39
Zn-N (2)	62.63 ^H	78.5 ^{A,1} , 86.0 ^{A,2}	2.00
Type I-J (N^*)	Morse: $U_{Zn-N} = \sum D_r (1 - e^{-\alpha(r_{ij} - r_{ij}^0)})^2$	$D_r / kcal mol^{-1}$	$r_{ij}^0 / \text{\AA}$
Zn-N (2)	29.25	1.87	2.00
ANGLE BENDING (12 types)			
	Harmonic: $U_{bend} = \sum k_\theta (\theta_{ijk} - \theta_{ijk}^0)^2$		

Table S.3 (continued)

Type I-J-K (N*)	intraZIF		AMBER	
	$k_\theta / \text{kcal mol}^{-1} \text{rad}^{-2}$	$k_\theta / \text{kcal mol}^{-1} \text{rad}^{-2}$	$\theta_{ijk}^0 / {}^\circ \text{degrees}$	
O-C4-H4 (1)	82.10	50.0	121.52	
O-C4-C1 (1)	104.06	80.0	124.02	
H4-C4-C1 (1)	98.74	50.0	114.47	
C4-C1-N (2)	129.33	70.0	124.18	
C1-N-C2 (2)	123.56	70.0	105.80	
N-C2-H2 (2)	64.50	50.0	121.64	
N-C2-C2 (2)	129.12	70.0	108.38	
N-C1-N (1)	94.24	70.0	111.63	
C2-C2-H2 (2)	68.10	50.0	129.97	
C1-N-Zn (2)	40.69 ^H /18.28 ^P	50.0	127.89	
C2-N-Zn (2)	41.06 ^H /18.84 ^P	35.0	126.05	
N-Zn-N (3)	30.68 ^H /18.20 ^P	10.5	109.46	

DIHEDRAL ANGLES (15 types)				
Type I-J-K-L (N*)	Cosine: $U_{proper} = \sum k_\phi [1 + \cos(m \phi_{ijkl} - \phi_{ijkl}^0)]$			
	intraZIF	AMBER	$\phi_{ijkl}^0 / {}^\circ \text{degrees}$	$m / -$
O-C4-C1-N (2)	2.02	2.325	180.0	2
H4-C4-C1-N (2)	1.39	2.325	180.0	2
C4-C1-N-C2 (2)	1.48±0.45	4.15	180.0	2
N-C1-N-C2 (2)	3.97	4.80	180.0	2
C2-C2-N-C1 (2)	2.72	4.80	180.0	2
H2-C2-N-C1 (2)	3.43	4.80	180.0	2
N-C2-C2-H2 (2)	2.61	4.00	180.0	2
N-C2-C2-N (1)	1.85	4.00	180.0	2
H2-C2-C2-H2 (1)	0.00	4.00	180.0	2
C4-C1-N-Zn (2)	0.00	NA	180.0	2
N-C1-N-Zn (2)	0.00	NA	180.0	2
C2-C2-N-Zn (2)	0.00	NA	180.0	2
H2-C2-N-Zn (2)	0.00	NA	180.0	2

Type I-J-K-L (N*)	Fourier series: $U_{proper} = \sum \sum_{n=1}^6 k_{\phi,n} [1 + \cos(m_n \phi_{ijkl} - d_n)]$			
	$k_\phi / \text{kcal mol}^{-1}$	$d_n / {}^\circ \text{degrees}$	$m / -$	
C1-N-Zn-N (6)	3.02±1.48, 2.26±1.42, 0.08±0.05	0.0, 180.0, 0.0	1, 2, 3	
C2-N-Zn-N (6)	3.39±0.74, 1.92±0.79, 0.02±0.02	0.0, 0.0, 0.0	1, 2, 3	

IMPROPER ANGLES (3 types)

Type I-J-K-L (N*)	Fourier series: $U_{improper} = \sum k_\xi [1 + \cos(m \xi_{ijkl} - \xi_{ijkl}^0)]$			
	intraZIF	AMBER	$\xi_{ijkl}^0 / {}^\circ \text{degrees}$	$m / -$
N-H2-C2 ^P -C2 (2)	0.00	1.10	180.0	2
C4-N-C1 ^P -N (1)	0.00	1.10	180.0	2
C1-C2-N ^P -Zn (2)	0.00	NA	180.0	2

Improper term I-J-K-L refers to the angle between planes I-J-K and J-K-L, with J-K axis of rotation and K being the central/primary atom (noted by subscript ^P); N*=number of bonds, angles, or dihedrals in the linker-metal complex. Superscripts H, P, and A refer to Hessian matrix, potential energy scan, or AMBER in reference to where certain spring constants were obtained.

Figure S.7a shows the single point potential energy scans for the Zn-N bond along with harmonic and Morse potential fits. **Figure S.7b** shows the contribution of the electrostatic energy for “fixed” and “varying” charges. **Figure S.8** shows the comparison of the **(a)** intraZIF-FF and **(b)** AMBER-FF predicted configurational potential energies from BOMD simulations on the cluster. **Figure S.9** shows the fitting of the rotation of the aldehyde group around the C₁-C₄ axis.

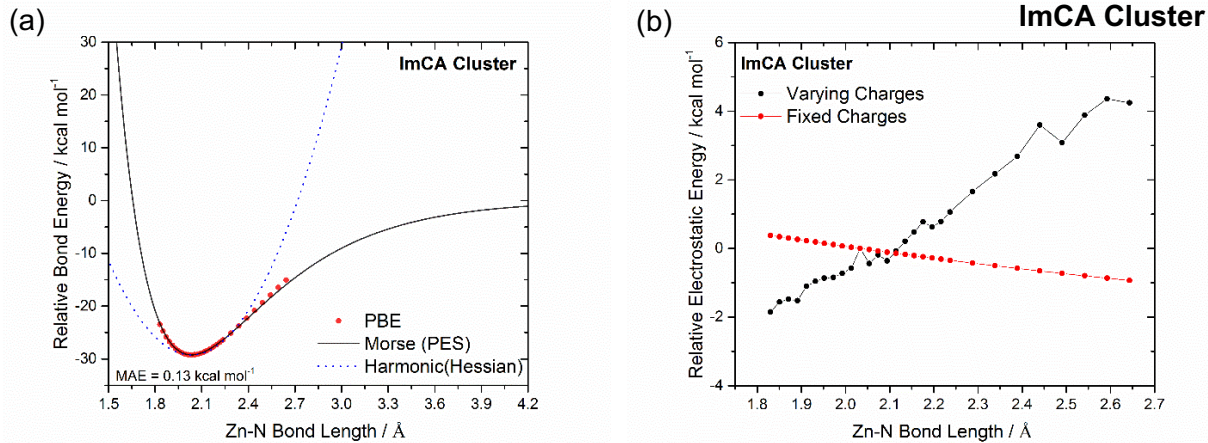


Figure S.7. **(a)** Morse potentials fit (solid black line) to potential energy scans (red dots) along the Zn-N bond. The harmonic potential with the spring constant from the Seminario method is shown for comparison (dashed blue line). The mean absolute error (MAE) of the Morse fit is also reported. **(b)** Relative coulombic energy for the Zn-N potential energy scans.

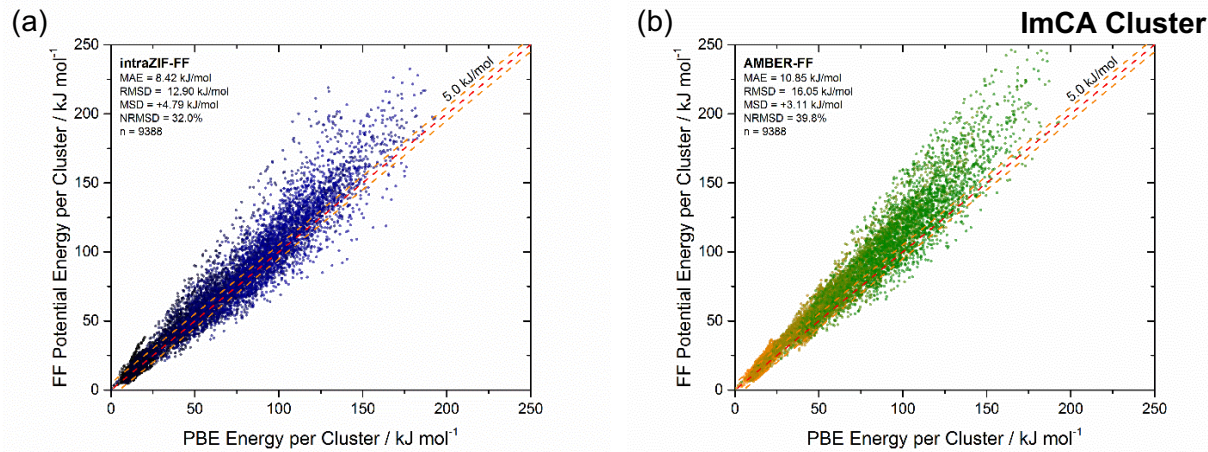


Figure S.8. Relative energy comparisons between PBE and **(a)** the intraZIF-FF including Fourier dihedrals from the potential energy fitting and **(b)** the AMBER-FF using standard cosine proper dihedrals. The color code (black to blue/intraZIF and orange to green/AMBER) is designed to easily identify the low and high energy regions.

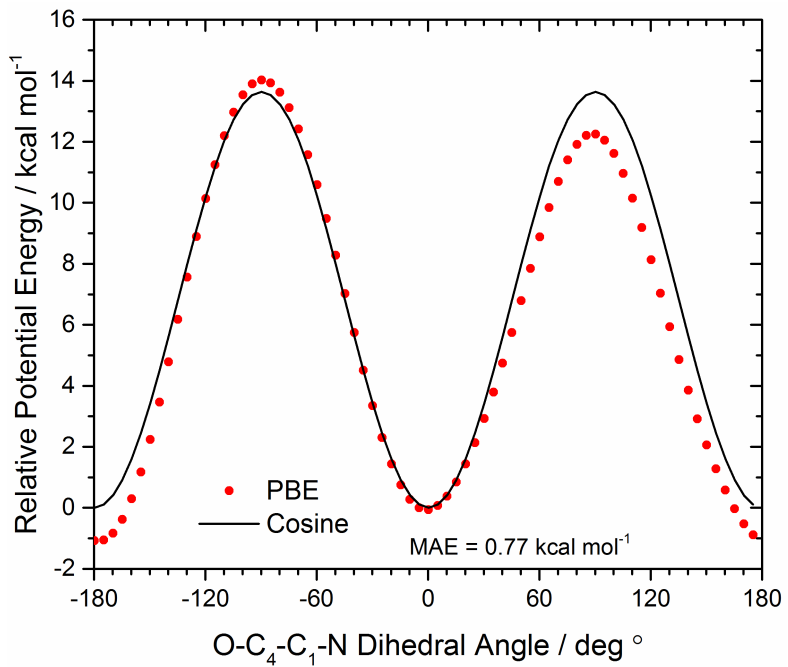
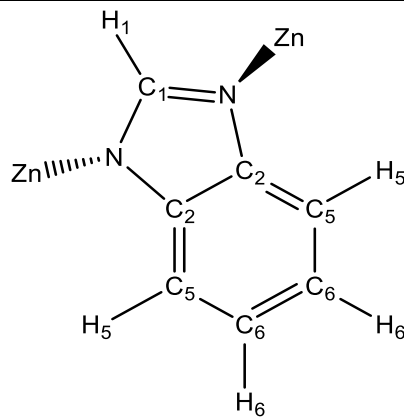


Figure S.9. Cosine potential fit of the PBE energies from potential energy scans involving rotation of the aldehyde group around the C₁-C₄ axis.

Benzimidazolate (BzIm) ZIF Intramolecular Force Field Parameters

Table S.4 below contains all the intramolecular force field functions and parameters implemented for ZIFs with benzimidazolate linkers. Green (red) shaded regions indicated which degrees of freedom are (not) included in the intraZIF-FF. Comparison of spring constants between the AMBER and intraZIF FFs are also included.

Table S.4. Bonded force field parameters for ZIFs with benzimidazolate linkers. Functional forms, spring constants, and equilibrium geometry parameters are listed.



BOND STRETCHES (10 types)			
Type I-J (N*)	Harmonic: $U_{stretching} = \sum k_r (r_{ij} - r_{ij}^0)^2$	intraZIF	AMBER
C ₁ -H ₁ (1)	369.37	367.0	1.09
C ₁ -N (2)	351.24	488.0	1.34
C ₂ -N (2)	274.22	410.0	1.39
C ₂ -C ₂ (1)	288.33	518.0	1.42
C ₂ -C ₅ (2)	350.29	469.0	1.40
C ₅ -H ₅ (2)	361.76	367.0	1.09
C ₅ -C ₆ (2)	366.93	469.0	1.39
C ₆ -H ₆ (2)	360.81	367.0	1.09
C ₆ -C ₆ (1)	339.98	469.0	1.41
Zn-N (2)	64.32 ^H	78.5 ^{A,1} , 86.0 ^{A,2}	1.99

Type I-J (N*)	Morse: $U_{Zn-N} = \sum D_r (1 - e^{-\alpha(r_{ij} - r_{ij}^0)})^2$	$D_r / kcal mol^{-1}$	$\alpha / \text{\AA}^{-1}$	$r_{ij}^0 / \text{\AA}$
Zn-N (2)		26.06	1.98	1.99

ANGLE BENDING (15 types)

Table S.4 (continued)

Type I-J-K (N*)	Harmonic: $U_{bend} = \sum k_\theta (\theta_{ijk} - \theta_{ijk}^0)^2$		
	intraZIF	AMBER	$\theta_{ijk}^0 / {}^\circ degrees$
	$k_\theta / kcal mol^{-1} rad^{-2}$	$k_\theta / kcal mol^{-1} rad^{-2}$	
N-C ₁ -H ₁ (2)	54.40	50.0	122.77
N-C ₁ -N (1)	113.26	70.0	114.47
N-C ₂ -C ₅ (2)	150.32	70.0	131.01
N-C ₂ -C ₂ (2)	121.99	70.0	107.68
C ₁ -N-C ₂ (2)	143.04	70.0	105.09
C ₂ -C ₅ -H ₅ (2)	60.12	50.0	121.52
C ₂ -C ₅ -C ₆ (2)	157.37	63.0	117.01
C ₅ -C ₆ -C ₆ (2)	190.48	63.0	121.67
C ₅ -C ₆ -H ₆ (2)	60.10	50.0	119.17
C ₆ -C ₆ -H ₆ (2)	60.55	50.0	119.15
C ₆ -C ₅ -H ₅ (2)	63.88	50.0	121.48
C ₂ -C ₂ -C ₅ (2)	145.80	63.0	120.93
N-Zn-N (3)	32.04 ^H /18.20 ^P	10.5	109.42
Zn-N-C ₁ (2)	49.24 ^H /18.28 ^P	50.0	126.76
Zn-N-C ₂ (2)	51.17 ^H /18.84 ^P	35.0	127.94

DIHEDRAL ANGLES (24 types)

Type I-J-K-L (N*)	Fourier series: $U_{proper} = \sum k_\phi [1 + \cos(m \phi_{ijkl} - \phi_{ijkl}^0)]$		
	intraZIF	AMBER	$m / -$
	$k_\phi / kcal mol^{-1}$	$k_\phi / kcal mol^{-1}$	
N-C ₂ -C ₅ -C ₆ (2)	0.38±0.36	4.80	180.0
H ₁ -C ₁ -N-C ₂ (2)	2.37±1.29	4.80	180.0
C ₁ -N-C ₂ -C ₂ (2)	0.69±0.57	4.80	180.0
H ₅ -C ₅ -C ₂ -N (2)	0.22±0.11	4.80	180.0
C ₂ -C ₂ -C ₅ -H ₅ (2)	0.26±0.19	4.80	180.0
C ₅ -C ₂ -C ₂ -C ₅ (1)	0.62±0.32	4.00	180.0
H ₅ -C ₅ -C ₆ -C ₆ (2)	0.22±0.21	4.80	180.0
H ₆ -C ₆ -C ₆ -C ₅ (2)	0.56±0.30	4.80	180.0
C ₅ -C ₆ -C ₆ -C ₅ (1)	1.06±1.10	4.80	180.0
N-C ₂ -C ₂ -N (1)	1.10±1.14	4.00	180.0
N-C ₂ -C ₂ -C ₅ (2)	0.49±0.41	4.00	180.0
C ₁ -N-C ₂ -C ₅ (2)	0.59±0.46	4.80	180.0
C ₂ -C ₅ -C ₆ -H ₆ (2)	1.24±1.33	4.80	180.0
C ₆ -C ₅ -C ₂ -C ₂ (2)	0.22±0.32	4.80	180.0
C ₆ -C ₆ -C ₅ -C ₂ (2)	0.58±0.44	4.80	180.0
N-C ₁ -N-C ₂ (2)	2.30±1.25	4.80	180.0
H ₅ -C ₅ -C ₆ -H ₆ (2)	0.00	4.80	180.0
H ₆ -C ₆ -C ₆ -H ₆ (1)	0.00	4.80	180.0
Zn-N-C ₁ -H ₁ (2)	0.00	NA	180.0
Zn-N-C ₂ -C ₅ (2)	0.00	NA	180.0
Zn-N-C ₁ -N (2)	0.00	NA	180.0
Zn-N-C ₂ -C ₂ (2)	0.00	NA	180.0

$$\text{Fourier series: } U_{proper} = \sum_{n=1}^6 k_{\phi,n} [1 + \cos(m_n \phi_{ijkl} - d_n)]$$

Type I-J-K-L (N*)	$k_\phi / kcal mol^{-1}$	$d_n / {}^\circ degrees$	$m / -$
C ₁ -N-Zn-N (6)	3.02±1.48, 2.26±1.42, 0.08±0.05	0.0, 180.0, 0.0	1, 2, 3

Table S.4 (continued)

C₂-N-Zn-N (6)

3.39±0.74, 1.92±0.79, 0.02±0.02

0.0, 0.0, 0.0

1, 2, 3

IMPROPER ANGLES (5 types)

$$\text{Fourier series: } U_{\text{improper}} = \sum k_\xi [1 + \cos(m \xi_{ijkl} - \xi_{ijkl}^0)]$$

intraZIF**AMBER**

Type I-J-K-L (N*)	$k_\xi / \text{kcal mol}^{-1}$	$k_\xi / \text{kcal mol}^{-1}$	$\xi_{ijkl}^0 / {}^\circ \text{degrees}$	$m / -$
-------------------	--------------------------------	--------------------------------	--	---------

N-C ₂ -C ₂ ^P -C ₅ (2)	0.00	1.10	180.0	2
H ₁ -N-C ₁ ^P -N (1)	0.00	1.10	180.0	2
H ₆ -C ₅ -C ₆ ^P -C ₆ (2)	0.00	1.10	180.0	2
H ₅ -C ₆ -C ₅ ^P -C ₂ (2)	0.00	1.10	180.0	2
C ₁ -C ₂ -N ^P -Zn (2)	0.00	NA	180.0	2

Improper term I-J-K-L refers to the angle between planes I-J-K and J-K-L, with J-K axis of rotation and K being the central atom (noted by subscript P); N*=number of bonds, angles, or dihedrals in the linker-metal complex. Superscripts H, P, and A refer to Hessian matrix, potential energy scan, or AMBER in reference to where certain spring constants were obtained.

Figure S.10a shows the single point potential energy scans for the Zn-N bond along with harmonic and Morse potential fits. **Figure S.10b** shows the contribution of the electrostatic energy for “fixed” and “varying” charges. **Figure S.11** shows the comparison of the **(a)** intraZIF-FF and **(b)** AMBER-FF predicted configurational potential energies from BOMD simulations on the cluster.

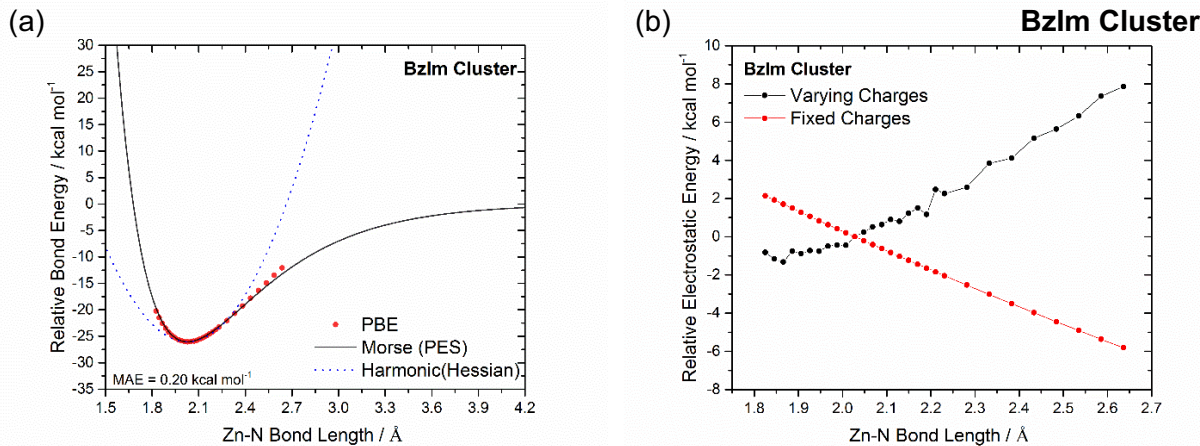


Figure S.10. **(a)** Morse potentials fit (solid black line) to potential energy scans (red dots) along the Zn-N bond. The harmonic potential with the spring constant from the Seminario method is shown for comparison (dashed blue line). The mean absolute error (MAE) of the Morse fit is also reported. **(b)** Relative coulombic energy for the Zn-N potential energy scans.

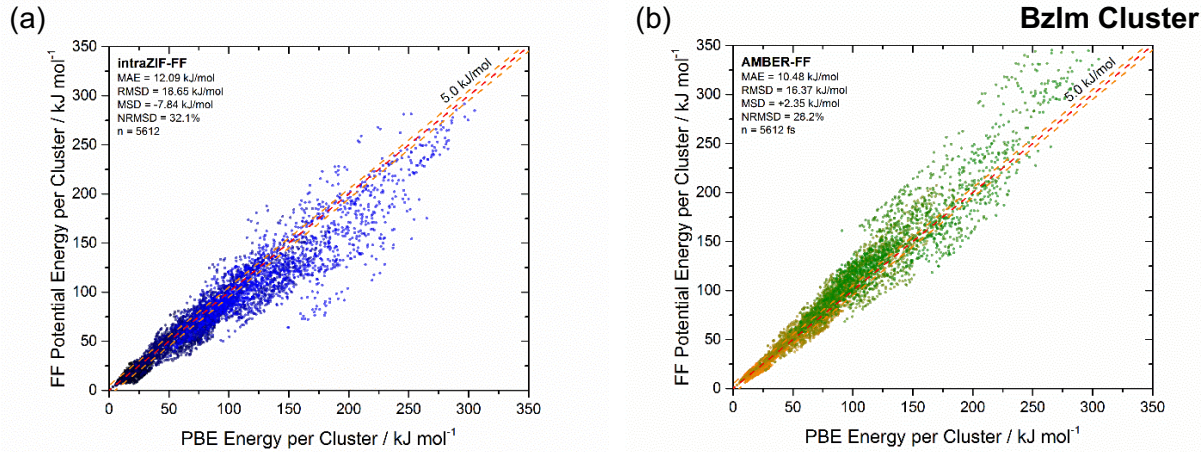


Figure S.11. Relative energy comparisons between PBE and **(a)** the intraZIF-FF including Fourier dihedrals from the potential energy fitting and **(b)** the AMBER-FF using standard cosine proper dihedrals. The color code (black to blue/intraZIF and orange to green/AMBER) is designed to easily identify the low and high energy regions.

Modeling Zn-N-C_{1,2} and N-Zn-N Bending by Fitting to Potential Energy Scans

Single point potential energy scans along the Zn-N-C_{1,2} and N-Zn-N bending degrees of freedom of the Im, mIm, BzIm, and ImCA clusters. The axis of rotation was defined as the normal vector to the plane formed by the three carbon atoms of the central linker's imidazolate five-member ring. The origin for the axis of rotation was defined as location of the N atom on the central linker for the Zn-N-C_{1,2} bending and the Zn atom for the N-Zn-N bending. To test how symmetrical the clusters were, two potential energy scans were performed on both N and Zn atoms of the ImCA cluster. The “O” and “H” subscripts on **Figures S.12** and **S.13** below indicate whether the N, Zn atoms closer to the O or H atoms on the aldehyde group respectively were used as the origin of rotation. The relative angle energy is a sum of all the angles changing in the scan.

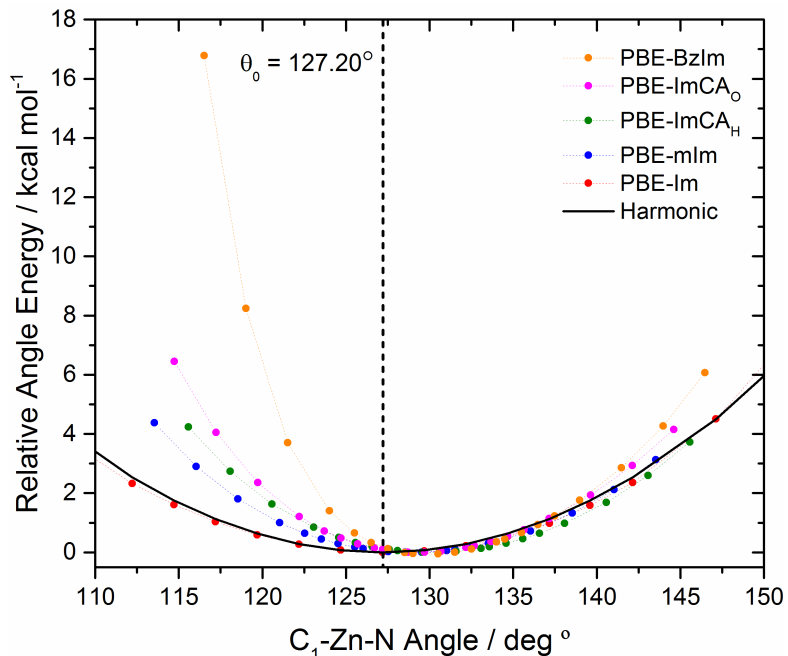


Figure S.12. Potential energy scan along the C_1 -Zn-N and C_2 -Zn-N angles for the four clusters with the harmonic fit to the unfunctionalized imidazolate cluster scan (black line).

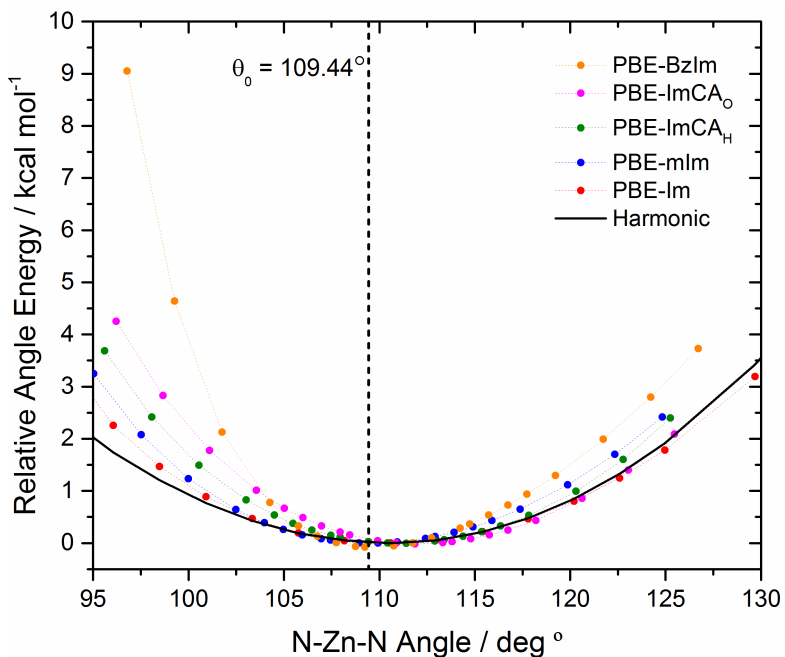


Figure S.13. Potential energy scan along the N-Zn-N angles for the four clusters with the harmonic fit to the unfunctionalized imidazolate cluster scan (black line).

Nonbonded Force Field Parameters for ZIFs

Van der Waals Pair-Wise Interactions

Adsorbent-adsorbent van der Waals interactions were modeled using a Buckingham potential (intraZIF-FF) and compared to 12-6 Lennard-Jones parameters from the AMBER-FF. All parameters are listed in **Tables S.5 and S.6**. Van der Waals parameters on the ZIF framework atoms for adsorbent-adsorbate interactions (**Table S.7**) were modeled using parameters from the Universal force field where all epsilon values were scaled by 0.54, which was demonstrated to more accurately reproduce N₂, CH₄, and CO₂ adsorption² and hydrocarbon diffusion in ZIF-8⁵. We have not parameterized any adsorbate-adsorbent interactions, instead using Lorentz-Berthelot mixing rules. This provides an easy and standard method for modeling framework-adsorbate interactions. For those seeking to parameterize more accurate adsorbate-adsorbent interactions, we direct the reader to a review article by Fang et al. detailing methods for developing force fields that model adsorbate-adsorbent interactions.⁶ To describe diffusion with true accuracy, adsorbate-adsorbent configurations at transition states (e.g. isobutane in the ZIF-8 window) must be included in any force field fitting procedure.

Since stretching and bending terms account for short range interactions, we chose to exclude bonded pairs (1-2 interactions) and valence angles (1-3 interactions) from van der Waals and electrostatic interactions. Pairs of atoms separated by three consecutive bonds (1-4 interactions) were also excluded from pair interactions. For comparison, the AMBER-FF⁷ scales the 1-4 van der Waals and electrostatic interactions by a factor of 1/2 and 5/6 respectively. Lorentz-Berthelot mixing rules were applied to generate van der Waals cross terms.

Table S.5. Buckingham potential parameters taken from the Molecular Mechanics 3 (MM3)⁸⁻⁹ force field and used in the intraZIF-FF.

Atom Type	ϵ_{ii} [kcal/mol]	r_{ii}^0 [\text{\AA}]
Zn	0.0276	2.29
N	0.043	1.93
C _{1,2,5,6}	0.056	1.94
C _{3,4}	0.027	2.04
H _{1,2,3,5,6}	0.020	1.50
H ₄	0.020	1.62
O	0.059	1.82

Table S.6. AMBER van der Waals parameters taken from the `parm10.dat` file.

Atom Type	ϵ [kcal/mol]	σ [\AA]
Zn	0.0125	1.96
N	0.1700	3.25
C _{1,2,3,4,5}	0.0860	3.40
H _{1,2,5,6}	0.0150	2.51
H _{3,4}	0.0157	2.65
O	0.2100	2.96

Table S.7. Unscaled and scaled epsilon and sigma 12-6 Lennard Jones parameters from the Universal Force Field (UFF) used to describe adsorbate-adsorbent interactions.

Atom Type	ϵ [kcal/mol]	0.54ϵ [kcal/mol]	σ [\AA]
Zn	0.124	0.067	2.462
N	0.069	0.037	3.261
C _x	0.105	0.057	3.431
H _x	0.044	0.024	2.571
O	0.060	0.032	3.118

Electrostatic Pair-Wise Interactions

Table S.8 shows the DDEC charges for periodic ZIFs used in the intraZIF-FF. **Table S.9** shows which pair-wise coulombic interactions include the Debye damping factor.

Table S.8. Charges for periodic ZIFs from the DDEC method used in the intraZIF-FF.

Atom Type	Im	BzIm	mIm	ImCA
Zn	0.7294	0.7826	0.7599	0.7136
N	-0.3621	-0.4502	-0.4312	-0.3455
C1	0.1636	0.2432	0.4280	0.1994
C2	-0.0529	0.1722	-0.0571	0.0095
C3	-	-	-0.4676	-
C4	-	-	-	0.2450
C5	-	-0.0881	-	-
C6	-	-0.1982	-	-
H1	0.0931	0.0988	-	-
H2	0.1043	-	0.1083	0.1096
H3	-	-	0.1399	-
H4	-	-	-	0.0459
H5	-	0.0988	-	-
H6	-	0.0988	-	-
O	-	-	-	-0.3942

Table S.9. Pair-wise coulombic interactions utilizing the Debye damping factor.

ZIF	Atom i (charge / e)	Atom j (charge / e)	Short Range Interaction
SALEM-2	Zn (+0.7294)	Zn (+0.7294)	Repulsive
	Zn (+0.7294)	C2 (-0.0529)	Attractive
ZIF-7	Zn (+0.7826)	Zn (+0.7826)	Repulsive
	Zn (+0.7826)	C2 (+0.1722)	Repulsive
	Zn (+0.7826)	C5 (-0.0881)	Attractive
ZIF-8	Zn (+0.7599)	Zn (+0.7599)	Repulsive
	Zn (+0.7599)	N (-0.4312)	Attractive
	Zn (+0.7599)	C1(+0.4280)	Repulsive
	Zn (+0.7599)	C2 (-0.0571)	Attractive
	Zn (+0.7599)	C3(-0.4676)	Attractive
	Zn (+0.7599)	H2(+0.1083)	Repulsive
	Zn (+0.7599)	H3(+0.1399)	Repulsive
ZIF-90	Zn (+0.7136)	Zn (+0.7136)	Repulsive
	Zn (+0.7136)	C1 (+0.1994)	Repulsive
	Zn (+0.7136)	C2 (+0.0095)	Repulsive

For those seeking to use the intraZIF-FF, below is the required LAMMPS setting for the Debye interactions:

```
##NONBONDED LAMMPS POTENTIAL PARAMETERS##
pair_style hybrid/overlay lj/cut 15.5 buck 15.5 coul/long 15.5 coul/debye 0.33 15.5
special_bonds lj 1.0e-10 1.0e-10 1.0e-10 coul 1.0e-10 1.0e-10 1.0e-10
kspace_style ewald/disp 1.0E-06
pair_modify tail yes
pair_modify pair coul/debye special coul 0.0 0.0 1.0
include VDW_LAMMPS.data
include CHARGES_LAMMPS.data
##END NONBONDED LAMMPS POTENTIAL PARAMETERS##
```

Figures S.14-S.17 compare the charges derived from the central linker in the clusters to charges derived from the periodic ZIFs.

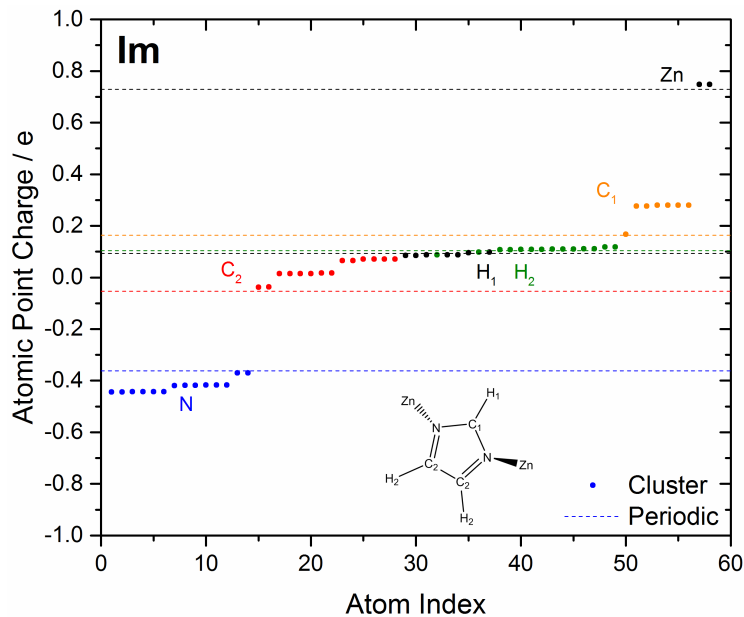


Figure S.14. Charges on individual atoms in the Im cluster as compared to periodic charges.

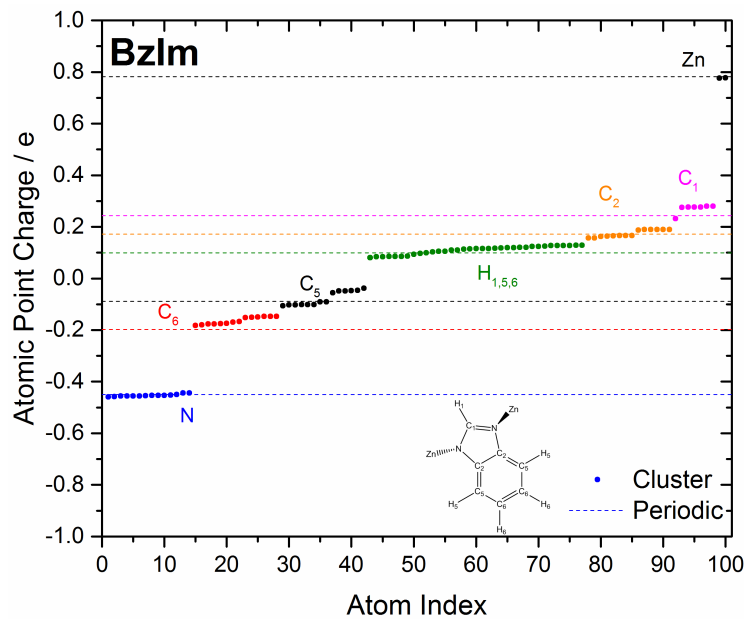


Figure S.15. Charges on individual atoms in the BzIm cluster as compared to periodic charges.

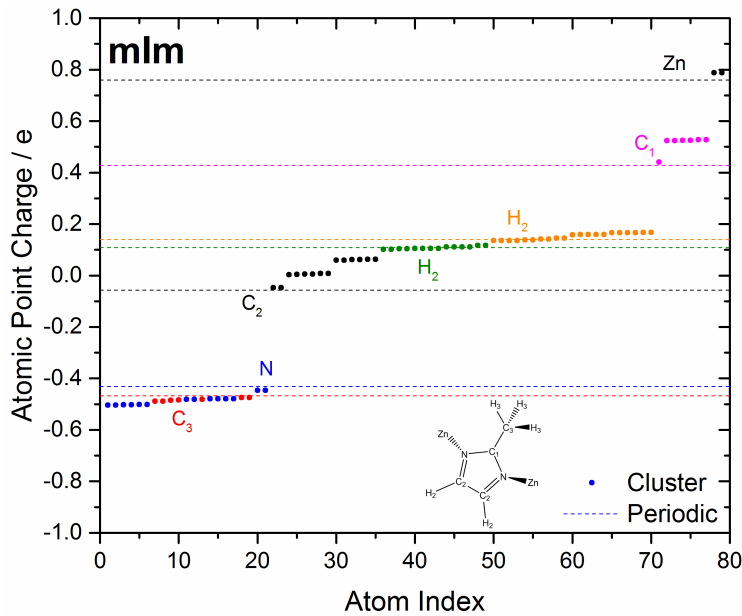


Figure S.16. Charges on individual atoms in the mIm cluster as compared to periodic charges.

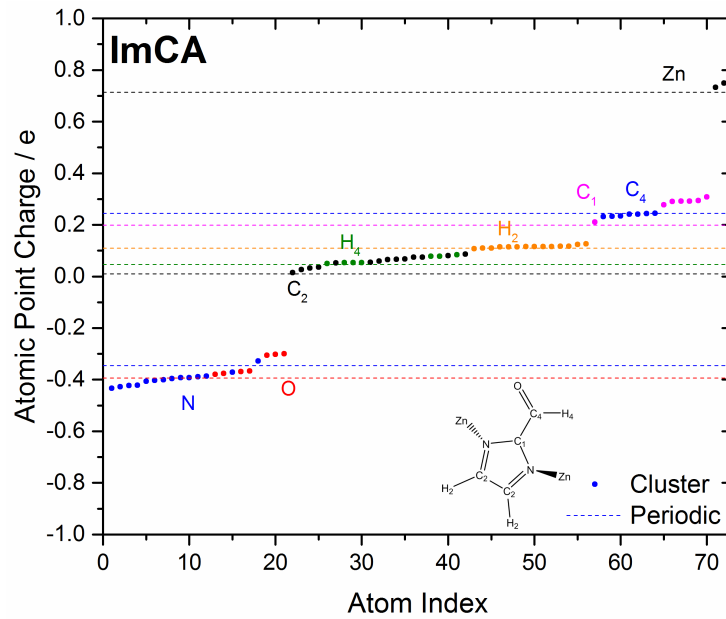


Figure S.17. Charges on individual atoms in the ImCA cluster as compared to periodic charges.

Geometric Predictions of SALEM-2, ZIF-7, ZIF-8, ZIF-90

Below in **Tables S.10-S.13**, we report the lattice parameters, pore limiting diameter (PLD), largest cavity diameter (LCD), accessible surface area (ASA), non-accessible surface area (NASA), accessible volume (AV), non-accessible volume (NAV), and density calculated using Zeo++ with a probe radius of 1.3 Å.¹⁰

Table S.10. SALEM-2 structural parameter comparisons between DFT and FF energy minimizations. ASA (NASA) and AV (NAV) are reported for the simulation volume (2x2x2 supercell).

Structural Parameter	PBE-D2	PBE-D3(BJ)	intraZIF	AMBER
a [Å]	16.84	16.86	16.83	16.55
b [Å]	16.84	16.86	16.83	16.48
c [Å]	16.84	16.86	16.83	16.51
PLD [Å]	3.15	3.17	3.54	3.16
LCD [Å]	11.74	11.75	11.52	10.86
ASA (NASA) [Å ²]	8004.72 (0)	8041.04 (0)	8206.25 (0)	7527.33 (0)
AV (NAV) [Å ³]	10775.36 (0)	10846.00 (0)	10561.4 (0)	8995.95 (0)
ρ [g cm ⁻³]	0.8326	0.8299	0.8337	0.8828

Table S.11. ZIF-7 structural parameter comparisons between DFT and FF energy minimizations. ASA (NASA) and AV (NAV) are reported for the simulation volume (2x2x2 supercell).

Structural Parameter	PBE-D2	PBE-D3(BJ)	intraZIF	AMBER
a [Å]	22.46	22.51	22.50	21.53
b [Å]	22.46	22.51	22.50	21.54
c [Å]	15.95	15.99	16.08	15.63
PLD [Å]	2.29	2.27	2.22	1.65
LCD [Å]	5.52	5.50	4.95	4.38
ASA (NASA) [Å ²]	0 (4899.51)	0 (4953.79)	0 (3963.8)	0 (2097.59)
AV (NAV) [Å ³]	0 (1767.99)	0 (1863.49)	0 (1093.92)	0 (481.195)
ρ [g cm ⁻³]	1.2855	1.2766	1.2707	1.4265

Table S.12. ZIF-8 structural parameter comparisons between DFT and FF energy minimizations. ASA (NASA) and AV (NAV) are reported for the simulation volume (2x2x2 supercell).

Structural Parameter	PBE-D2	PBE-D3(BJ)	intraZIF	AMBER
a [Å]	16.94	16.98	16.90	16.46
b [Å]	16.94	16.98	16.91	16.46
c [Å]	16.94	16.98	16.90	16.46
PLD [Å]	3.31	3.32	3.44	3.05
LCD [Å]	11.39	11.42	10.89	10.91
ASA (NASA) [Å ²]	6976.22 (0)	6987.86 (0)	7038.57 (0)	6156.93 (0)
AV (NAV) [Å ³]	9109.63 (0)	9222.16 (0)	8670.51 (0)	7246.57 (0)
ρ [g cm ⁻³]	0.9324	0.9271	0.9390	1.0169

Table S.13. ZIF-90 structural parameter comparisons between DFT and FF energy minimizations. ASA (NASA) and AV (NAV) are reported for the simulation volume (2x2x2 supercell).

Structural Parameter	PBE-D2	PBE-D3(BJ)	intraZIF	AMBER
a [Å]	17.14	17.20	17.34	16.97
b [Å]	17.16	17.22	17.29	16.98
c [Å]	17.05	17.11	17.09	16.55
PLD [Å]	3.45	3.49	3.77	3.40
LCD [Å]	10.91	10.97	10.95	10.30
ASA (NASA) [Å²]	7245.54 (0)	7304.22 (0)	7661.72 (0)	6916.94 (0)
AV (NAV) [Å³]	9376.08 (0)	9612.72 (0)	9470.43 (0)	7727.50 (0)
ρ [g cm ⁻³]	1.0151	1.0046	0.9940	1.0678

Im and mIm ZIF Polymorphs: Geometric and Stability Predictions

Tables S.14 and S.15 show the PLDs and accessible surfaces respectively of the PBE-D2, PBE-D3(BJ), the intraZIF-FF, and the AMBER-FF energy optimized Im polymorphs. **Tables S.16 and S.17** show the PLDs and accessible surfaces respectively of the PBE-D2, PBE-D3(BJ), the intraZIF-FF, and the AMBER-FF energy optimized mIm polymorphs. **Figure S.18** shows the parity plots for **(a)** unit cell densities and **(b)** LCDs as predicted by PBE-D2 and the intraZIF and AMBER force fields.

Table S.14. Pore limiting diameters [Å] of Im polymorphs listed in alphabetical order.

Polymorph	PBE-D2	PBE-D3(BJ)	intraZIF	AMBER
afw	3.93	3.90	3.78	3.25
cag_exp	2.11	2.11	1.92	2.00
cfc	4.58	4.58	3.88	4.02
coe	2.40	2.36	2.24	2.06
crb_exp	5.12	5.12	4.96	4.66
dft_exp	5.60	5.60	4.56	5.62
dia	3.98	3.98	3.78	3.79
gis_exp	5.37	5.37	5.60	5.78
gsi	2.41	2.40	2.26	2.24
irl	2.34	2.33	2.36	2.02
lcs	2.76	2.76	3.22	2.66
lon	4.47	4.46	4.54	3.50
lta	9.04	9.06	9.22	7.39
mer_exp	7.58	7.59	7.46	6.69
mmt	3.30	3.30	3.30	2.82
neb	2.30	2.31	2.44	2.44
pcb	5.63	5.63	6.32	5.46
pcl	6.54	6.52	6.69	5.44
qtz	3.82	3.73	2.92	2.08
sod	3.39	3.39	3.42	3.44
sra	6.79	6.87	6.81	5.01
unc	4.69	4.70	4.45	3.82
unh	8.86	8.86	8.77	8.85
uni	7.00	7.01	6.75	6.66
unj	6.49	6.44	5.93	6.68
uoc	4.33	4.33	4.52	3.84
zni_exp	2.40	2.40	1.59	2.11

Table S.15. Accessible surface areas [m^2/cm^3] per unit cell of Im polymorphs listed in alphabetical order.

Polymorph	PBE-D2	PBE-D3(BJ)	intraZIF	AMBER
afw	2638.22	2626.04	2611.59	2143.95
cag_exp	0	0	0	0
cfc	2360.46	2366.97	2299.06	1851.99
coe	0	0	0	0
crb_exp	2454.38	2454.60	2546.25	2217.79
dft_exp	2475.44	2475.80	2468.06	2269.16
dia	2410.58	2413.00	2286.11	2160.64
gis_exp	2434.78	2434.68	2352.52	2332.26
gsi	0	0	0	0
irl	0	0	0	0
lcs	1825.88	1830.81	2183.13	1429.30
lon	2320.14	2323.24	2291.85	1904.69
lta	1735.93	1733.54	1725.08	1775.87
mer_exp	2236.55	2237.10	2243.45	2197.59
mmt	1935.19	1940.68	1918.98	620.652
neb	0	0	0	0
pcb	2399.10	2399.19	2304.84	2368.83
pcl	2502.03	2503.26	2433.51	2208.51
qtz	3019.71	3015.36	1642.29	0
sod	2090.02	2088.74	2152.79	2125.25
sra	2510.26	2511.82	2437.83	2303.12
unc	1582.40	1596.55	1530.85	1119.69
unh	1838.93	1839.39	1929.91	1755.20
uni	1277.84	1278.16	1218.88	1152.15
unj	1553.01	1524.95	1570.54	1542.67
uoc	2471.62	2476.30	2473.89	2306.17
zni_exp	0	0.00	0	0

Table S.16. Pore limiting diameters [\AA] of mIm polymorphs listed in alphabetical order.

Polymorph	PBE-D2	PBE-D3(BJ)	intraZIF	AMBER
cag	3.18	3.21	3.37	2.46
cfc	3.21	3.21	3.17	3.05
coi	1.15	1.18	1.33	1.12
crb	4.00	3.96	4.37	3.94
dft	5.56	5.58	5.44	6.46
dia	1.66	1.69	1.57	1.36
gis	7.04	7.06	7.07	6.38
gsi	2.15	2.17	2.06	1.71
irl	3.10	3.08	2.65	2.28
lcs	2.96	2.97	3.36	2.42
lon	3.16	3.21	3.15	2.83
lta	7.11	7.14	7.08	6.88
mer	7.61	7.69	7.41	7.18
mmt	1.66	1.70	1.43	1.57
neb	1.91	1.96	1.76	1.35
pcb	5.90	6.06	6.29	5.63
pcl	5.56	5.58	5.28	4.96
qtz	2.12	2.19	2.08	1.14
sod	3.20	3.20	3.30	3.05
sra	6.33	6.39	5.98	5.87
unc	4.73	4.86	4.97	4.43
unh	7.66	7.52	7.75	7.53
uni	5.14	5.28	5.06	4.83
unj	5.98	5.91	5.67	5.74
zni	1.35	1.36	1.10	1.07

Table S.17. Accessible surface areas [m²/cm³] per unit cell of mIm polymorphs listed in alphabetical order.

Polymorph	PBE-D2	PBE-D3(BJ)	intraZIF	AMBER
cag	2106.68	2120.01	2018.05	0
cfc	1733.02	1770.02	1672.21	1277.91
coi	0	0.00	0	0
crb	956.277	959.53	928.74	896.423
dft	2008.39	2024.84	1929.82	1884.71
dia	0	0	0	0
gis	1991.79	1992.04	1954.44	1960.52
gsi	0	0	0	0
irl	1252.53	1266.31	927.183	0
lcs	1298.88	1313.57	1458.14	0
lon	1823.6	1863.03	1789.27	1240.99
lta	1666.26	1666.18	1600.35	1638.78
mer	2002.26	1998.65	1951.01	1936.13
mmt	0	0	0	0
neb	0	0	0	0
pcb	2145.14	2137.28	2078.04	2032.57
pcl	2059.46	2067.06	2034.1	1939.3
qtz	0	0.00	0	0
sod	1766.77	1767.72	1795.15	1726.43
sra	2108.41	2110.03	2052.57	1930.88
unc	1024.83	1094.01	1018.65	944.765
unh	1675.84	1643.96	1508.06	1646.08
uni	709.902	717.81	568.809	594.674
unj	1557.88	1540.00	1494.24	1509.49
zni	0	0	0	0

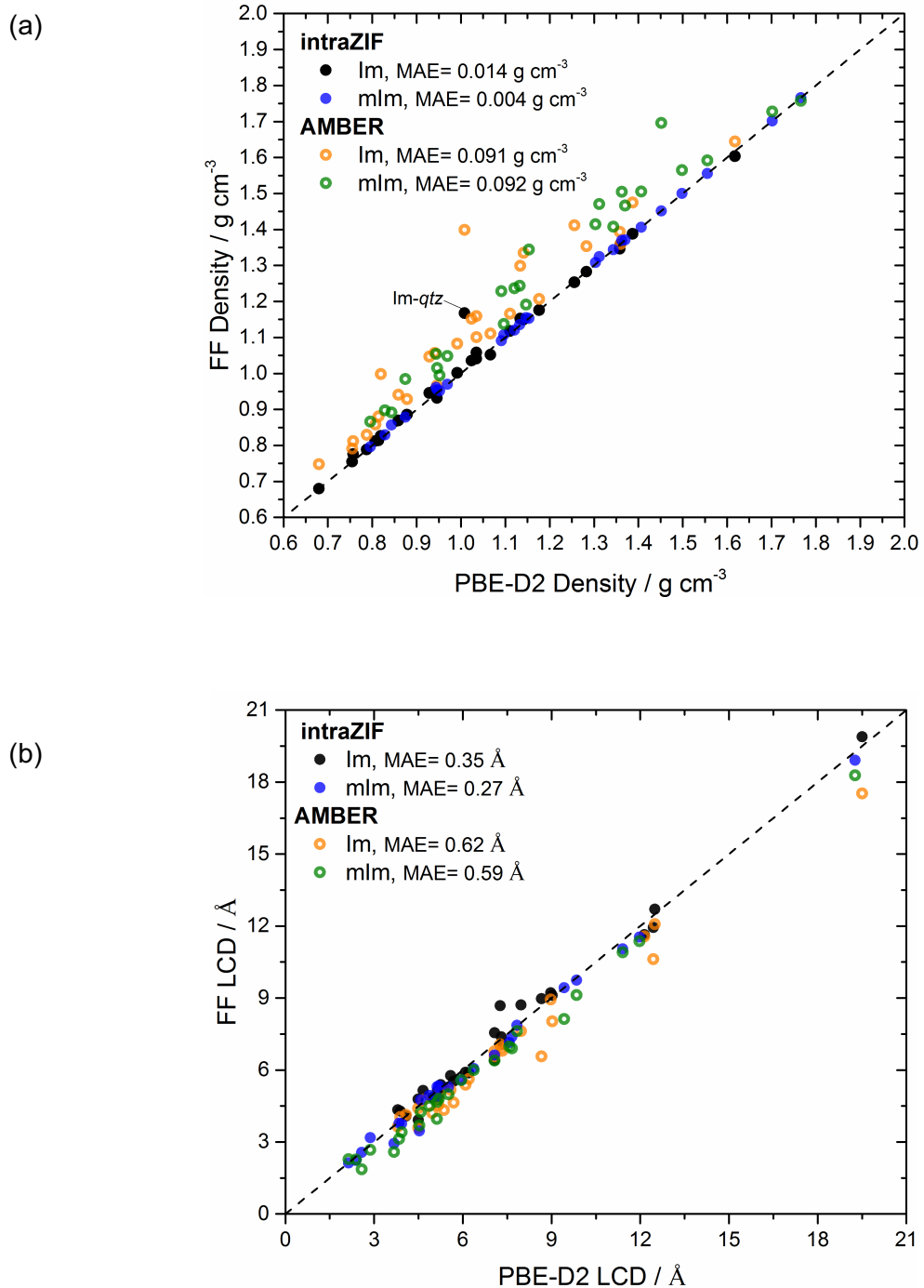


Figure S.18. Parity plots for (a) unit cell densities and (b) LCDs as predicted by PBE-D2 and the intraZIF (blue/black) and AMBER (orange/green) force fields. There are 27 Im polymorphs as well as the SALEM-2 structure (closed circles) and 25 mIm polymorphs (open circles).

Figure S.19 below shows the minimum, maximum, and average N-Zn-N angle for the 27 Im polymorphs as well as SALEM-2. **Figure S.20** shows the coordination environment for two different Im polymorphs.

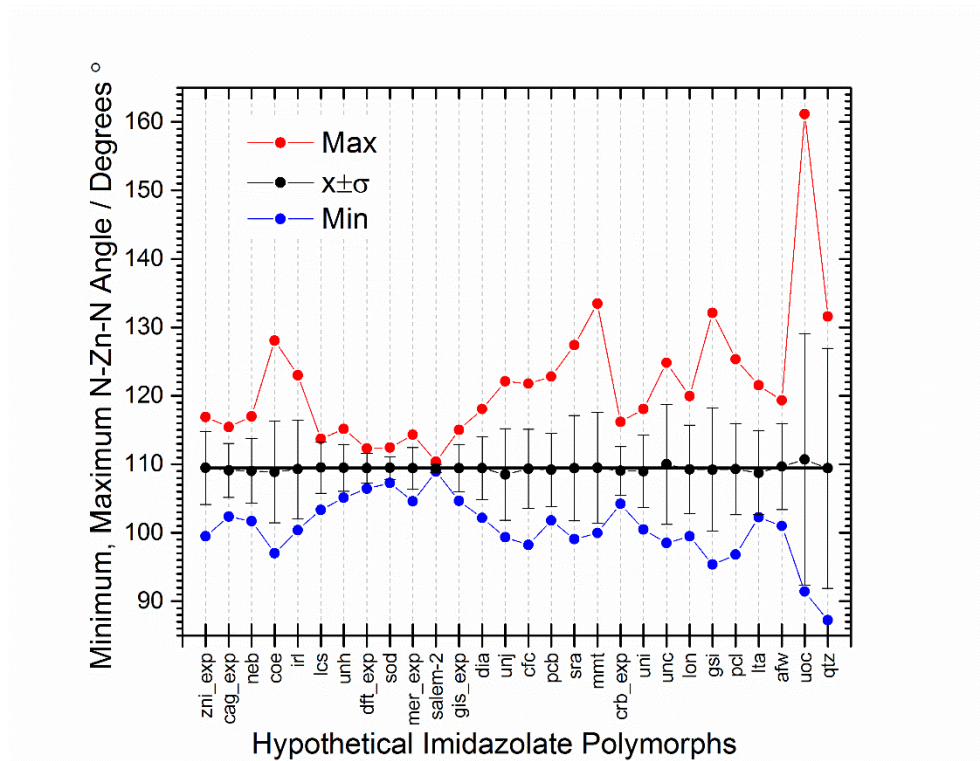


Figure S.19. Analysis of N-Zn-N angles in the 27 Im polymorphs and SALEM-2. Error bars on the average (black solid circles) represent the standard deviation of all the N-Zn-N angles in the unit cell.

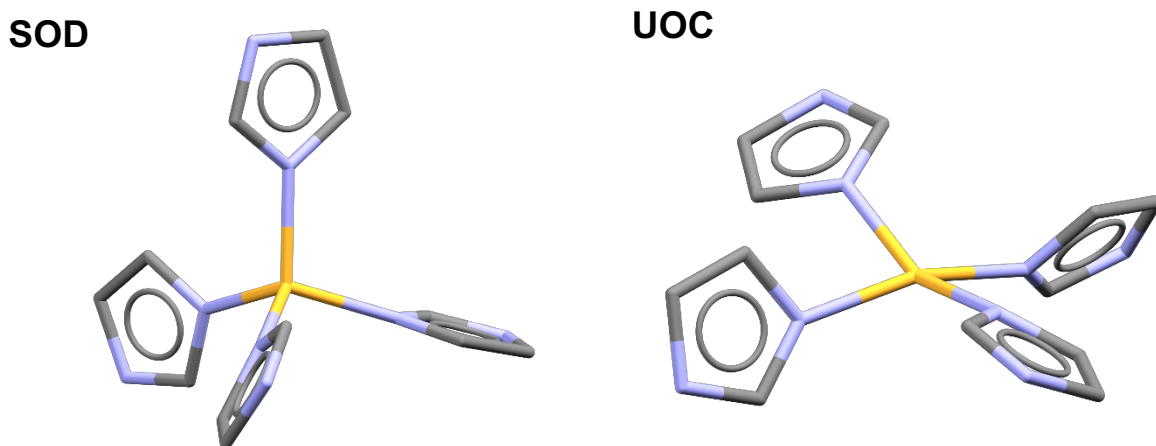


Figure S.20. Examples of tetrahedral and near square planar Zn coordination environments for the Im-sod and Im-uoc polymorphs.

Tables S.18 and S.19 show the relative configuration energies for Im and mIm polymorphs with the *zni* polymorph as the reference.

Table S.18. Relative configurational energies [kJ/mol/Zn] of Im polymorphs ranked according to the PBE-D2 predicted stabilities.

Polymer	PBE-D2	PBE-D3(BJ)	intraZIF	AMBER
zni_exp	0.0	0.0	0.0	0.0
cag_exp	17.2	14.9	8.4	12.2
neb	18.0	18.4	12.3	17.0
coe	21.0	20.0	10.0	17.7
irl	22.2	22.8	12.6	16.0
lcs	24.3	20.8	10.0	25.0
unh	27.2	26.1	10.9	26.0
dft_exp	27.2	24.3	7.4	26.9
sod (SALEM-2)	27.3	24.4	4.7	28.7
mer_exp	27.3	24.8	6.7	29.4
gis_exp	27.9	25.5	5.0	32.3
dia	28.8	27.8	5.1	25.4
unj	29.0	28.3	13.2	22.1
cfc	30.2	29.2	7.3	24.4
pcb	30.3	27.6	7.6	30.6
sra	30.8	29.7	9.2	28.1
mmt	31.4	30.9	13.8	23.5
crb_exp	31.6	30.4	7.2	25.5
uni	31.9	30.9	11.7	24.9
unc	32.3	30.4	7.0	22.1
lon	32.9	33.5	12.1	26.5
gsi	33.3	31.9	14.0	23.7
pcl	33.9	32.5	5.5	25.6
lta	40.5	40.9	17.0	35.7
afw	44.8	45.5	13.3	36.2
uoc	54.3	55.7	24.0	45.6
qtz	93.4	96.4	12.8	15.3

Table S.19. Relative configurational energies [kJ/mol/Zn] of mIm polymorphs ranked according to the PBE-D2 predicted stabilities.

Polymorph	PBE-D2	PBE-D3(BJ)	intraZIF	AMBER
dia	-5.0	-6.7	11.6	-26.3
zni	0.0	0.0	0.0	0.0
crb	3.3	0.4	23.0	-14.5
unc	6.4	3.0	22.6	-10.9
coi	7.3	12.5	11.4	15.5
sod (ZIF-8)	9.8	3.6	42.1	-10.2
qtz	12.4	5.1	10.8	-23.5
unj	17.2	16.4	39.3	8.0
mmt	18.6	16.6	13.4	-2.5
cag	19.8	17.4	46.0	4.0
gis	21.1	18.5	63.5	12.6
cfc	21.2	14.2	42.7	0.4
uni	21.3	16.4	19.8	-12.2
irl	22.0	19.0	36.1	4.0
mer	22.0	21.2	56.4	9.8
sra	22.3	19.5	47.3	13.4
lon	22.3	15.5	45.1	2.7
neb	23.7	20.3	25.6	-2.2
pcl	24.1	19.7	50.3	12.3
dft	27.1	23.2	60.0	14.7
gsi	28.3	23.8	29.1	5.0
pcb	29.4	26.9	58.3	13.0
lcs	36.6	32.2	47.1	-0.6
lta	46.1	41.5	63.7	20.6
unh	72.7	74.4	81.1	80.3

Born-Oppenheimer Molecular Dynamics (BOMD) Data for SALEM-2, ZIF-7, ZIF-8, and ZIF-90

The sections below show analysis of the BOMD simulations involving the periodic ZIF structures. This analysis examines some combination of relative potential energies, atomic forces, N-Zn bond lengths, and N-Zn-N angle bending for each structure in order to compare the intraZIF-FF to the AMBER-FF as well as justify the functional form of the intraZIF-FF. **This BOMD data was not used to fit the intraZIF-FF and is only used as reference data for benchmarking.**

SALEM-2 BOMD ANALYSIS

For the SALEM-2 structure, we have made comparisons between atomic forces predicted by the AMBER-FF (light green) and the intraZIF-FF (light blue) in reference to PBE-D3(BJ) forces from BOMD simulations at 700 K and 1.0 bar. These comparisons are shown in **Tables S.20-S.25** for

the six atom types. The force components are labeled x, y, z while mag stands for the force magnitude. Units are either in $\text{kJ mol}^{-1} \text{\AA}^{-1}$ (MAE, MSD, RMSD) or percentages (NRMSD). **Figure S.21** shows the temperature dependence of the SALEM-2 unit-cell volume using PBE-D3(BJ) and the intraZIF and AMBER FFs.

Table S.20. Force comparisons for the Zn atom type (n=97992) of the AMBER and intraZIF FFs to BOMD forces.

AMBER	Fx_MAE	Fy_MAE	Fz_MAE	Fmag_MAE
	41.60	42.43	43.47	59.35
Fx_MSD	Fy_MSD	Fz_MSD	Fmag_MSD	
-0.04	-1.49	-0.53	51.33	
Fx_RMSD	Fy_RMSD	Fz_RMSD	Fmag_RMSD	
53.95	55.33	56.49	75.18	
Fx_NRMSD	Fy_NRMSD	Fz_NRMSD	Fmag_NRMSD	
65.56	66.67	69.21	127.51	
intraZIF	Fx_MAE	Fy_MAE	Fz_MAE	Fmag_MAE
	33.07	34.37	34.30	50.75
Fx_MSD	Fy_MSD	Fz_MSD	Fmag_MSD	
2.47	1.20	-1.47	48.46	
Fx_RMSD	Fy_RMSD	Fz_RMSD	Fmag_RMSD	
41.90	43.45	43.07	60.41	
Fx_NRMSD	Fy_NRMSD	Fz_NRMSD	Fmag_NRMSD	
50.92	52.35	52.76	102.46	

MAE, MSD, and RMSD have units of $\text{kJ mol}^{-1} \text{\AA}^{-1}$; NRMSD is a percent.

Table S.21. Force comparisons for the N atom type (n=391968) of the AMBER and intraZIF FFs to BOMD forces.

AMBER	Fx_MAE	Fy_MAE	Fz_MAE	Fmag_MAE
	53.92	54.02	54.35	65.10
Fx_MSD	Fy_MSD	Fz_MSD	Fmag_MSD	
0.87	0.90	-0.60	35.32	
Fx_RMSD	Fy_RMSD	Fz_RMSD	Fmag_RMSD	
70.53	70.14	71.20	86.03	
Fx_NRMSD	Fy_NRMSD	Fz_NRMSD	Fmag_NRMSD	
51.16	50.63	51.99	83.41	
intraZIF	Fx_MAE	Fy_MAE	Fz_MAE	Fmag_MAE
	45.00	44.28	44.95	46.90
Fx_MSD	Fy_MSD	Fz_MSD	Fmag_MSD	
0.08	-0.08	0.02	-3.12	
Fx_RMSD	Fy_RMSD	Fz_RMSD	Fmag_RMSD	
57.29	56.05	56.96	60.16	
Fx_NRMSD	Fy_NRMSD	Fz_NRMSD	Fmag_NRMSD	
41.55	40.46	41.59	58.33	

MAE, MSD, and RMSD have units of $\text{kJ mol}^{-1} \text{\AA}^{-1}$; NRMSD is a percent.

Table S.22. Force comparisons for the C₁ atom type (n=195984) of the AMBER and intraZIF FFs to BOMD forces.

AMBER	Fx_MAE	Fy_MAE	Fz_MAE	Fmag_MAE
	57.48	56.54	56.02	69.49
Fx_MSD	Fy_MSD	Fz_MSD	Fmag_MSD	
1.68	0.18	-2.86	42.73	
Fx_RMSD	Fy_RMSD	Fz_RMSD	Fmag_RMSD	
74.75	73.15	72.77	91.78	
Fx_NRMSD	Fy_NRMSD	Fz_NRMSD	Fmag_NRMSD	
46.64	46.50	44.45	74.73	
intraZIF	Fx_MAE	Fy_MAE	Fz_MAE	Fmag_MAE
	51.50	49.57	50.52	55.44
Fx_MSD	Fy_MSD	Fz_MSD	Fmag_MSD	
1.02	0.10	-3.10	7.95	
Fx_RMSD	Fy_RMSD	Fz_RMSD	Fmag_RMSD	
65.82	63.12	64.32	71.58	
Fx_NRMSD	Fy_NRMSD	Fz_NRMSD	Fmag_NRMSD	
41.07	40.12	39.29	58.28	

MAE, MSD, and RMSD have units of $\text{kJ mol}^{-1} \text{\AA}^{-1}$; NRMSD is a percent.

Table S.23. Force comparisons for the C₂ atom type (n=391968) of the AMBER and intraZIF FFs to BOMD forces.

AMBER	Fx_MAE	Fy_MAE	Fz_MAE	Fmag_MAE
	57.17	56.41	57.92	72.18
Fx_MSD	Fy_MSD	Fz_MSD	Fmag_MSD	
0.07	2.12	0.34	53.28	
Fx_RMSD	Fy_RMSD	Fz_RMSD	Fmag_RMSD	
73.99	73.50	75.66	94.71	
Fx_NRMSD	Fy_NRMSD	Fz_NRMSD	Fmag_NRMSD	
46.69	46.34	47.01	74.50	
intraZIF	Fx_MAE	Fy_MAE	Fz_MAE	Fmag_MAE
	60.35	60.14	61.22	69.87
Fx_MSD	Fy_MSD	Fz_MSD	Fmag_MSD	
0.99	2.80	-0.34	34.73	
Fx_RMSD	Fy_RMSD	Fz_RMSD	Fmag_RMSD	
77.39	77.49	79.33	91.11	
Fx_NRMSD	Fy_NRMSD	Fz_NRMSD	Fmag_NRMSD	
48.83	48.85	49.29	71.67	

MAE, MSD, and RMSD have units of $\text{kJ mol}^{-1} \text{\AA}^{-1}$; NRMSD is a percent.

Table S.24. Force comparisons for the H₁ atom type (n=195984) of the AMBER and intraZIF FFs to BOMD forces.

AMBER	Fx_MAE	Fy_MAE	Fz_MAE	Fmag_MAE
	18.33	17.51	18.43	23.26
Fx_MSD	Fy_MSD	Fz_MSD	Fmag_MSD	
-0.44	0.19	2.05	10.70	
Fx_RMSD	Fy_RMSD	Fz_RMSD	Fmag_RMSD	
28.58	29.35	34.50	44.30	
Fx_NRMSD	Fy_NRMSD	Fz_NRMSD	Fmag_NRMSD	
32.91	36.43	38.02	55.71	
intraZIF	Fx_MAE	Fy_MAE	Fz_MAE	Fmag_MAE
	17.52	16.35	17.36	21.39
Fx_MSD	Fy_MSD	Fz_MSD	Fmag_MSD	
-0.11	0.87	1.91	7.63	
Fx_RMSD	Fy_RMSD	Fz_RMSD	Fmag_RMSD	
24.47	22.37	24.59	31.86	
Fx_NRMSD	Fy_NRMSD	Fz_NRMSD	Fmag_NRMSD	
28.18	27.76	27.10	40.06	

MAE, MSD, and RMSD have units of $\text{kJ mol}^{-1} \text{\AA}^{-1}$; NRMSD is a percent.

Table S.25. Force comparisons for the H₂ atom type (n=391968) of the AMBER and intraZIF FFs to BOMD forces.

AMBER	Fx_MAE	Fy_MAE	Fz_MAE	Fmag_MAE
	22.46	22.61	22.36	28.04
Fx_MSD	Fy_MSD	Fz_MSD	Fmag_MSD	
-1.54	-2.84	0.77	17.18	
Fx_RMSD	Fy_RMSD	Fz_RMSD	Fmag_RMSD	
31.07	32.37	33.64	43.51	
Fx_NRMSD	Fy_NRMSD	Fz_NRMSD	Fmag_NRMSD	
36.69	36.49	40.22	53.13	
intraZIF	Fx_MAE	Fy_MAE	Fz_MAE	Fmag_MAE
	26.14	26.50	26.10	32.80
Fx_MSD	Fy_MSD	Fz_MSD	Fmag_MSD	
-2.14	-3.50	1.26	22.35	
Fx_RMSD	Fy_RMSD	Fz_RMSD	Fmag_RMSD	
35.45	36.22	35.08	46.02	
Fx_NRMSD	Fy_NRMSD	Fz_NRMSD	Fmag_NRMSD	
41.87	40.83	41.94	56.21	

MAE, MSD, and RMSD have units of $\text{kJ mol}^{-1} \text{\AA}^{-1}$; NRMSD is a percent.

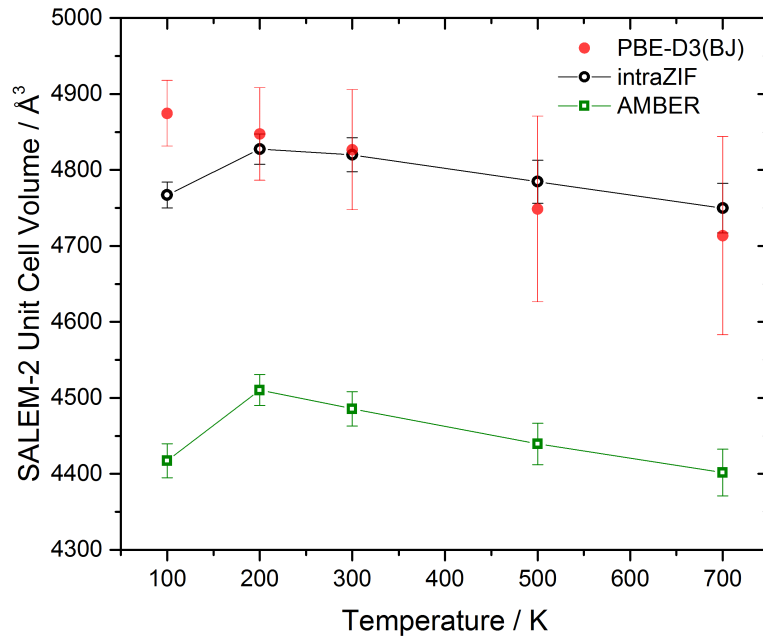


Figure S.21. Temperature dependence of the SALEM-2 unit-cell volume using PBE-D3(BJ), the intraZIF-FF, and the AMBER-FF. The mean and standard deviations at each temperature point were obtained by averaging the volume over the production duration of the NPT-MD simulations.

ZIF-8 BOMD Analysis

For the ZIF-8 structure, we have made comparisons between the relative potential energies from BOMD simulations and the AMBER-FF as well as the intraZIF-FF as shown in **Figure S.22**.

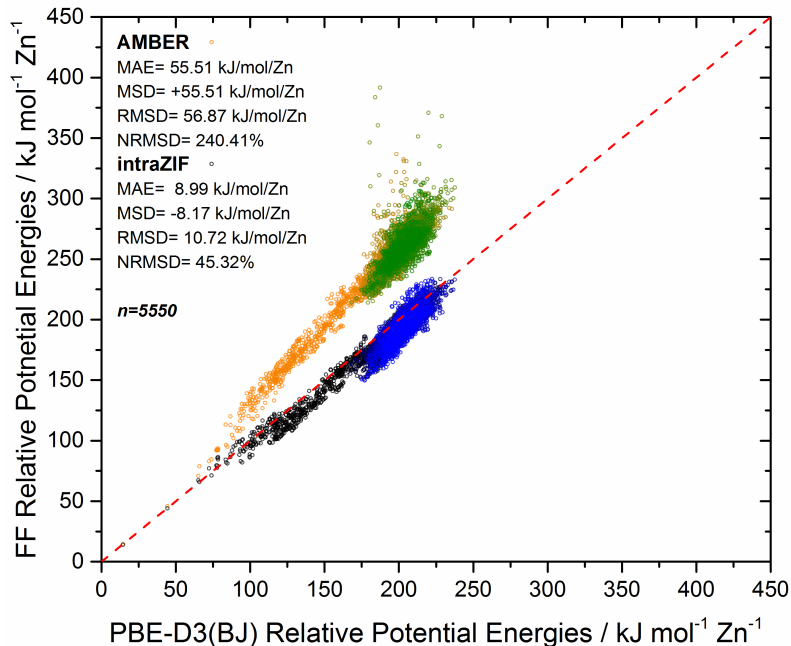


Figure S.22. ZIF-8 relative potential energies as predicted by the AMBER-FF and intraZIF-FF in reference to PBE-D3(BJ) relative energies from fully periodic BOMD simulations at 700 K and 1.01 bar.

ZIF-90 BOMD Analysis

For the ZIF-90 structure, we have made comparisons between the relative potential energies from BOMD simulations and the AMBER-FF as well as the intraZIF-FF as shown in **Figure S.23**. We also examined the Zn-N stretch and the N-Zn-N bend as a function of temperature to verify the functional form used in the intraZIF-FF as shown in **Figure S.24**.

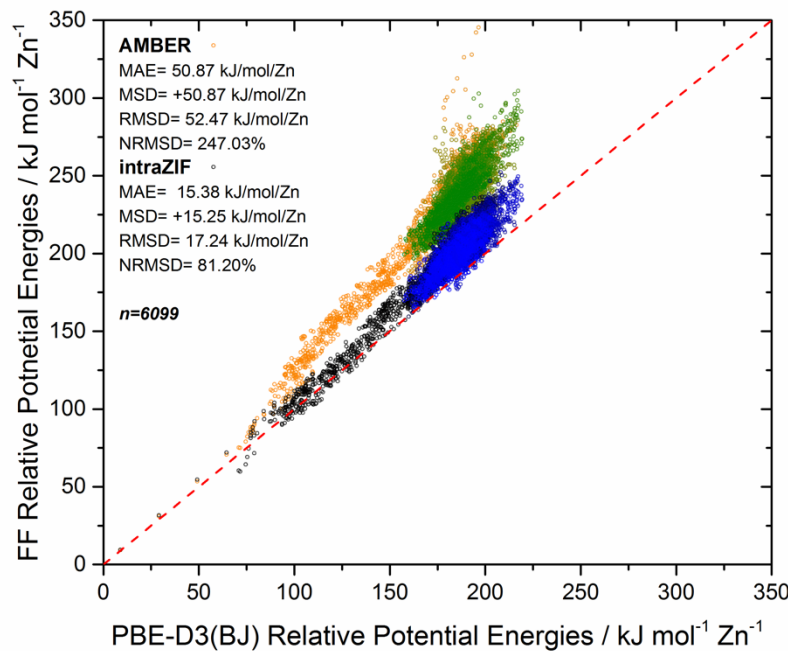
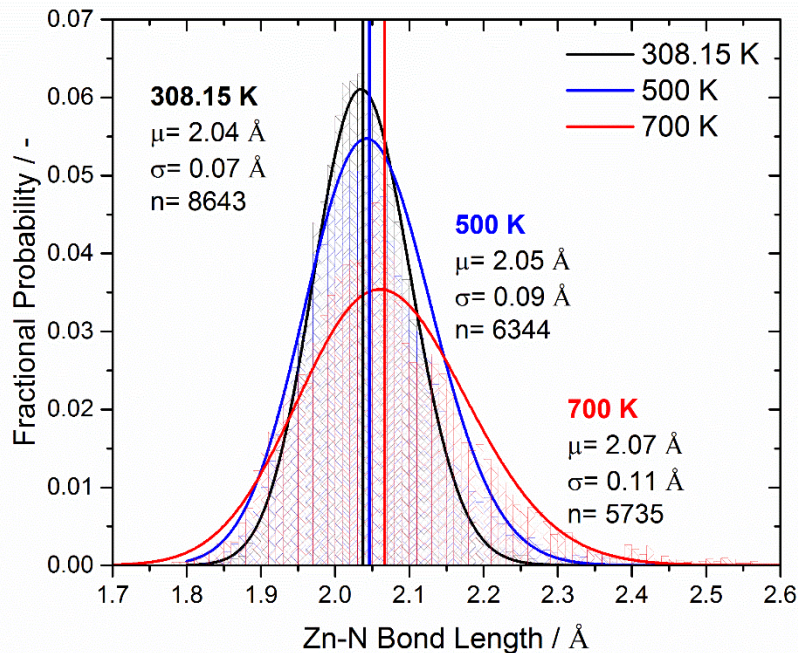


Figure S.23. ZIF-90 relative potential energies as predicted by the AMBER-FF and intraZIF-FF in reference to PBE-D3(BJ) relative energies from fully periodic BOMD simulations at 700 K and 1.01 bar.

(a)



(b)

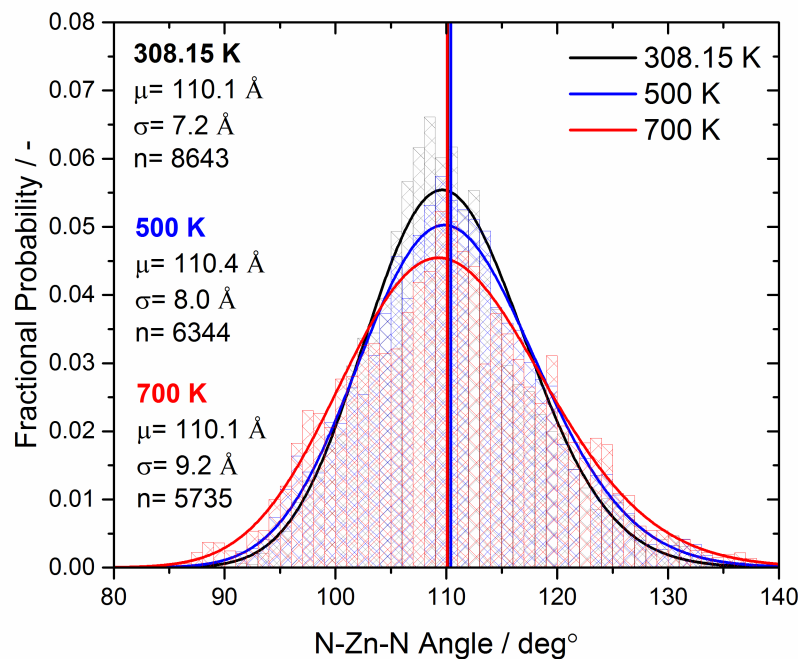


Figure S.24. Histograms with fitted lognormal distributions of (a) Zn-N bond lengths and (b) N-Zn-N angles in ZIF-90 at temperatures of 308.15, 500, and 700 K and a pressure of 1.0 bar. Mu (μ), sigma (σ) are the mean and standard deviation of the lognormal distribution and n is the number of samples.

ZIF-7 BOMD Analysis

For the ZIF-7 structure, we have made comparisons between the relative potential energies from BOMD simulations and the AMBER-FF as well as the intraZIF-FF as shown in **Figure S.25**.

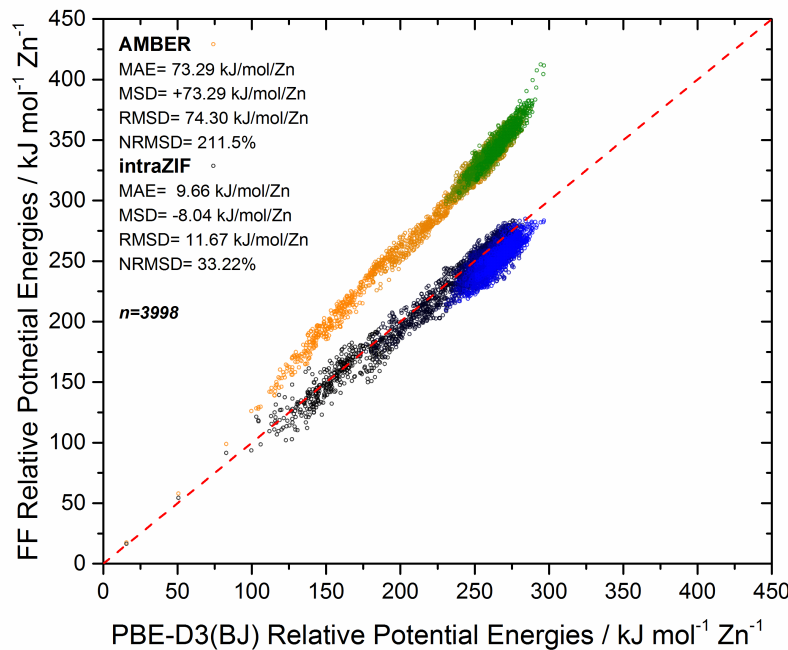
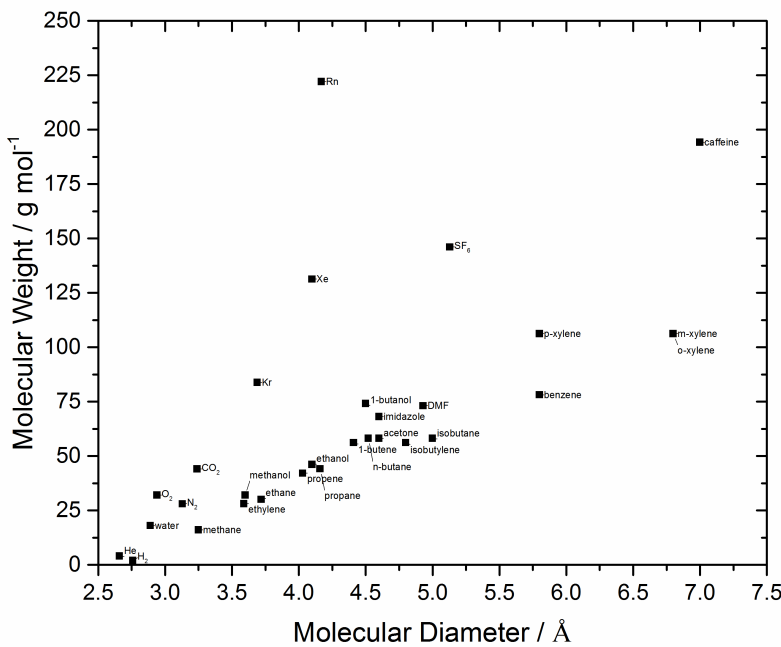


Figure S.25. ZIF-7 relative potential energies as predicted by the AMBER-FF and intraZIF-FF in reference to PBE-D3(BJ) relative energies from fully periodic BOMD simulations at 700 K and 1.01 bar.

Light Gas Diffusion in SALEM-2, ZIF-8, ZIF-90, and ZIF-7

Adsorbate Force Fields

We examined five single-site 12-6 LJ fluids of increasing molecular size (He^{11} , Kr^{12} , Xe^{12} , Rn^{12} , and SF_6^{13}) as well as four small 3-site rigid linear molecules (H_2^{14} , O_2^{15} , $\text{N}_2^{2,16}$, CO_2^{17}). We also modeled thirteen alcohols, paraffins, and olefins using the united atom TraPPE FF¹⁸⁻²⁰: CH_3OH (methanol), $\text{C}_2\text{H}_5\text{OH}$ (ethanol), $\text{C}_4\text{H}_9\text{OH}$ (1-butanol), $\text{CH}_3\text{-CO-CH}_3$ (acetone)²¹, CH_4 , $\text{C}_2\text{H}_4=$, C_2H_6 , $\text{C}_3\text{H}_6=$, C_3H_8 , $1\text{-C}_4\text{H}_8=$, $n\text{-C}_4\text{H}_{10}$, iso- $\text{C}_4\text{H}_8=$, and iso- C_4H_{10} . The single and double C-C bonds were modeled with a harmonic potential²², a departure from the original TraPPE implementation to facilitate implementation in LAMMPS. The OPLS force field was used to model rigid C_6H_6 , m- C_8H_{10} , o- C_8H_{10} , and p- C_8H_{10} .²³⁻²⁴ We also examined water, N,N-dimethylformamide (DMF), imidazole, and 1,3,7-trimethylxanthine (caffeine, $\text{C}_8\text{H}_{10}\text{N}_4\text{O}_2$). We have also included H_2O modeled using the SPC/E FF designed to work with long range electrostatic solvers (Ewald).²⁵⁻²⁶ N,N-Dimethylformamide (DMF) was modeled using the six-interaction site OPLS model (CS2) by Chalaris and Samios.²⁷ Imidazole was modeled using the explicit hydrogen TraPPE FF.²⁸ 1,3,7-trimethylxanthine (caffeine, $\text{C}_8\text{H}_{10}\text{N}_4\text{O}_2$) was modeled using the rigid force field of Sanjeewa and Weerasinghe with the methyl functionalities as united atom groups.²⁹ A hybrid approach was adopted for determining molecular diameters. Molecular diameter definitions include kinetic diameters (KD), van der Waals diameters (vdW), as well as Lennard-Jones (LJ) diameters. **Figure S.26** shows the adsorbates examined according to their molecular diameter and molecular weight. **Table S.26** shows all the adsorbate LJ parameters. For those seeking to replicate these calculations, the bond lengths, angles, and dihedrals used are in the original references.



			H	1.01	0.0	0.0	0.0	0.435
12	C ₂ H ₅ OH	4.10 ^{KD,32}	CH ₃ _sp3	15.03	3.750	0.1947	98.0	0.0
			CH ₂ _sp3 ^a	14.02	3.950	0.0914	46.0	0.265
			O	16.00	3.020	0.1848	93.0	-0.700
			H	1.01	0.0	0.0	0.0	0.435
13	CH ₄	3.25 ^{vdWD,30}	CH ₄	16.04	3.73	0.2941	148.0	0.0
14	C ₂ H ₄ =	3.59 ^{vdWD,30}	2xCH ₂	14.02	3.675	0.1689	85.0	0.0
15	C ₂ H ₆	3.72 ^{vdWD,30}	2xCH ₃	15.03	3.750	0.1947	98.0	0.0
16	C ₃ H ₆ =	4.03 ^{vdWD,30}	CH ₂	14.02	3.675	0.1689	85.0	0.0
			CH	13.02	3.730	0.0934	47.0	0.0
			CH ₃	15.03	3.750	0.1947	98.0	0.0
17	C ₃ H ₈	4.16 ^{vdWD,30}	CH ₃	15.03	3.750	0.1947	98.0	0.0
			CH ₂	14.02	3.950	0.0914	46.0	0.0
18	1-C ₄ H ₈ =	4.41 ^{vdWD,30}	CH ₂	14.02	3.675	0.1689	85.0	0.0
			CH	13.02	3.730	0.0934	47.0	0.0
			CH ₂	14.02	3.950	0.0914	46.0	0.0
			CH ₃	15.03	3.750	0.1947	98.0	0.0
19	n-C ₄ H ₁₀	4.52 ^{vdWD,30}	2x CH ₃	15.03	3.750	0.1947	98.0	0.0
			2xCH ₂	14.02	3.950	0.0914	46.0	0.0
20	iso-C ₄ H ₈ =	4.8 ^{KD,30}	2xCH ₃	15.03	3.750	0.1947	98.0	0.0
			C	12.01	3.850	0.0397	20.0	0.0
			CH ₂	14.02	3.675	0.1689	85.0	0.0
21	iso-C ₄ H ₁₀	5.0 ^{KD,30}	CH ₃ _sp3	15.03	3.750	0.1947	98.0	0.0
			CH_sp3	13.02	4.680	0.0199	10.0	0.0
22	C ₆ H ₆	5.80 ^{KD,31}	6xC_xy1	12.01	3.55	0.0700	35.24	-0.115
			6xH_xy1	1.01	2.42	0.0299	15.03	0.115
23	m-C ₈ H ₁₀	6.80 ^{KD,31}	6xC_xy1	12.01	3.55	0.0700	35.24	-0.115
			4xH_xy1	1.01	2.42	0.0299	15.03	0.115
			2xCH ₃ _xy1	15.03	3.80	0.1699	85.51	0.115
24	o-C ₈ H ₁₀	6.80 ^{KD,31}	6xC_xy1	12.01	3.55	0.0700	35.24	-0.115
			4xH_xy1	1.01	2.42	0.0299	15.03	0.115
			2xCH ₃ _xy1	15.03	3.80	0.1699	85.51	0.115
25	p-C ₈ H ₁₀	5.80 ^{KD,31}	6xC_xy1	12.01	3.55	0.0700	35.24	-0.115
			4xH_xy1	1.01	2.42	0.0299	15.03	0.115
			2xCH ₃ _xy1	15.03	3.80	0.1699	85.51	0.115
26	(CH ₃) ₂ NC(O)H	4.93 ^{vdWD}	2xCH ₃ _dmf	15.03	3.80	0.1600	80.0	0.28
	DMF		N_dmf	14.01	3.20	0.1600	80.0	-0.57
			C_dmf	12.01	3.70	0.100	50.0	0.45
			O_dmf	16.00	2.96	0.2000	100.0	-0.50
			H_dmf	1.01	2.20	0.0160	8.0	0.06
27 ^{EH}	C ₃ H ₄ N ₂	4.6 ^{LJ}	N1_im	14.01	3.40	0.2820	141.0	-0.416
			C2_im	12.01	3.60	0.0614	30.7	0.224
			N3_im	14.01	3.20	0.1140	57.0	-0.485
			C4_im	12.01	3.60	0.0614	30.7	0.005
			C5_im	12.01	3.60	0.0614	30.7	0.030
			H6_im	1.01	0.50	0.0240	12.0	0.336
			H7_im	1.01	2.360	0.0510	25.5	0.097
			H8_im	1.01	2.360	0.0510	25.5	0.092
			H9_im	1.01	2.360	0.0510	25.5	0.117
28	1-butanol	4.5 ^{LJ}	CH ₃	15.03	3.75	0.1947	98.0	0.00
			2xCH ₂	14.02	3.95	0.0914	46.0	0.00
			CH ₂ _sp3 ^a	14.02	3.95	0.0914	46.0	0.265
			O	16.00	3.02	0.1848	93.0	-0.700

Table S.26 (continued)

			H	1.01	0.0	0.0	0.0	0.435
29	acetone	4.6 ^{LJ}	2xCH ₃ _sp ^{3k}	15.03	3.750	0.1947	98.0	0.00
			C_sp ^{2k}	12.01	3.820	0.0795	40.0	0.424
			O	16.00	3.050	0.1570	79.0	-0.424
30	caffeine	7.0 ^{LJ}	N1_caf	14.01	3.341	0.10466	52.67	-0.8395
			C2_caf	12.01	3.581	0.0908	45.69	0.9538
			N3_caf	14.01	3.341	0.10466	52.67	-0.7907
			C4_caf	12.01	3.581	0.0908	45.69	0.7944
			C5_caf	12.01	3.581	0.0908	45.69	0.3580
			C6_caf	12.01	3.581	0.0908	45.69	0.9451
			N7_caf	14.01	3.341	0.10466	52.67	-0.7854
			C8_caf	12.01	3.581	0.0908	45.69	0.4905
			N9_caf	14.01	3.341	0.10466	52.67	-0.6598
			C10_caf	12.01	3.581	0.0663	33.36	0.2768
			O11_caf	16.00	2.76	0.3057	153.8	-0.6036
			C12_caf	12.01	3.581	0.0663	33.36	0.2827
			O13_caf	16.00	2.76	0.3057	153.8	-0.7090
			C14_caf	12.01	3.581	0.0663	33.36	0.2866

Free Energy Barriers for SALEM-2, ZIF-8, and ZIF-90

Table S.27. Free energy barriers (FEB) for adsorbates in SALEM-2, ZIF-8, and ZIF-90 at 308 K and 1.01 bar.

Adsorbate	Im FEB [kJ mol ⁻¹]	mIm FEB [kJ mol ⁻¹]	ImCA FEB [kJ mol ⁻¹]
He	8.7	10.4	8.6
H ₂	10.0	11.0	9.3
H ₂ O	10.9	13.3	17.1
O ₂	11.5	13.8	12.0
N ₂	14.2	17.6	14.5
CO ₂	12.1	14.4	19.8
Methane	15.4	20.7	15.3
Ethylene	18.1	25.0	17.7
Methanol	14.0	20.8	18.8
Kr	15.3	19.6	13.9
Ethane	19.3	26.6	18.9
Propylene	20.9	31.4	21.3
Xe	19.6	32.6	24.4
Ethanol	18.4	32.2	25.2
Propane	22.8	37.6	26.5
Rn	19.3	35.3	24.2
1-Butene	23.3	37.9	26.3
1-Butanol	23.2	39.7	30.4
<i>n</i> -butane	23.9	39.2	26.5
Acetone	24.4	49.2	39.5
Imidazole	23.9	48.0	38.1
Isobutylene	30.7	57.9	49.3
DMF	25.3	61.9	60.0
Isobutane	34.0	66.7	57.3
SF ₆	36.2	71.4	64.1
Benzene	37.5	72.6	60.6
<i>p</i> -xylene	35.6	70.3	56.5
<i>m</i> -xylene	39.8	133.1	114.8
<i>o</i> -xylene	41.7	92.9	78.3
Caffeine	49.0	150.0	128.1

Dynamical Correction Factors for SALEM-2, ZIF-8, and ZIF-90

Table S.28. Dynamical correction factors for adsorbates in SALEM-2, ZIF-8, and ZIF-90 at 308 K and 1.01 bar. Poor statistics were obtained for the dynamical correction factors of three adsorbate-ZIF pairs and have been omitted.

Adsorbate	Im DCF [-]	mIm DCF [-]	ImCA DCF [-]
He	0.85	0.88	0.95
H ₂	0.77	0.88	0.89
H ₂ O	0.35	0.83	0.70
O ₂	0.74	0.90	0.90
N ₂	0.66	0.87	0.91
CO ₂	0.47	0.75	0.84
Methane	0.61	0.84	0.90
Ethylene	0.64	0.86	0.88
Methanol	0.38	0.29	0.11
Kr	0.67	0.86	0.88
Ethane	0.64	0.83	0.83
Propylene	0.60	0.70	0.78
Xe	0.58	0.75	0.85
Ethanol	0.37	0.44	0.68
Propane	0.59	0.59	0.74
Rn	0.59	0.57	0.85
1-Butene	0.56	0.39	0.72
1-Butanol	0.40	0.52	0.42
<i>n</i> -butane	0.63	0.66	0.63
Acetone	0.33	0.11	0.60
Imidazole	--	0.18	0.27
Isobutylene	0.53	0.04	0.05
DMF	0.07	--	--
Isobutane	0.26	0.01	0.01
SF ₆	0.40	0.36	0.34
Benzene	0.48	0.60	0.47
<i>p</i> -xylene	0.44	0.48	0.42
<i>m</i> -xylene	0.08	0.02	0.22
<i>o</i> -xylene	0.30	0.07	0.02
Caffeine	0.07	0.004	0.24

Self-Diffusion Coefficients for SALEM-2, ZIF-8, and ZIF-90

Table S.29. Self-diffusion coefficients for adsorbates in SALEM-2, ZIF-8, and ZIF-90 at 308 K and 1.01 bar.

Adsorbate	Im $D_{self} [\text{cm}^2 \text{s}^{-1}]$	mIm $D_{self} [\text{cm}^2 \text{s}^{-1}]$	ImCA $D_{self} [\text{cm}^2 \text{s}^{-1}]$
He	3.42E-04	2.11E-04	4.28E-04
H ₂	2.71E-04	2.43E-04	4.54E-04
H ₂ O	3.13E-05	3.97E-05	5.86E-06
O ₂	3.50E-05	2.00E-05	4.74E-05
N ₂	1.39E-05	5.42E-06	1.77E-05
CO ₂	1.69E-05	1.22E-05	2.53E-06
Methane	1.19E-05	1.95E-06	2.14E-05
Ethylene	3.55E-06	2.93E-07	5.72E-06
Methanol	7.83E-06	5.29E-07	5.45E-07
Kr	6.52E-06	1.37E-06	1.58E-05
Ethane	2.38E-06	1.55E-07	3.28E-06
Propylene	1.04E-06	1.73E-08	9.75E-07
Xe	8.88E-07	8.10E-09	2.57E-07
Ethanol	1.60E-06	7.85E-09	2.26E-07
Propane	4.15E-07	1.32E-09	1.39E-07
Rn	6.49E-07	1.38E-09	1.71E-07
1-Butene	3.18E-07	7.00E-10	1.53E-07
1-Butanol	2.08E-07	4.11E-10	1.40E-08
<i>n</i> -butane	2.88E-07	6.45E-10	9.26E-08
Acetone	1.03E-07	2.34E-12	6.00E-10
Imidazole	--	5.43E-12	6.98E-10
Isobutylene	2.09E-08	2.51E-14	9.88E-13
DMF	1.32E-08	--	--
Isobutane	2.91E-09	3.80E-16	1.38E-14
SF ₆	1.17E-09	9.28E-16	1.67E-14
Benzene	1.19E-09	1.09E-15	1.86E-13
<i>p</i> -xylene	1.60E-09	2.02E-15	5.94E-13
<i>m</i> -xylene	5.11E-11	1.66E-27	4.08E-23
<i>o</i> -xylene	7.49E-11	3.92E-20	5.95E-18
Caffeine	1.39E-12	4.91E-31	2.37E-25

Comparison to Prior Experimental Diffusion Data

Table S.30 shows a comparison between simulated diffusivities and those experimentally measured by Zhang et al.³² **Figure S.27** show a comparison between simulated diffusivities and those measured experimentally by Zhang et al.³², Eum et al.³³, and Zhang et al.³⁰ **Figure S.28** shows the Gibbs free energy barriers as a function of temperature for benzene and p-xylene.

Table S.30. Comparisons of simulated diffusivities to the experimental diffusivities measured by Zhang et al.³² The experimental diffusivities are measured at 50 °C and the simulated diffusivities are calculated at 35 °C.

Adsorbate	Experimental Data ³² [cm ² s ⁻¹]	NPT-MD (intraZIF-FF) [cm ² s ⁻¹]
water	2.2x10 ⁻⁷	3.97x10 ⁻⁵
ethanol	3.9x10 ⁻⁸	7.85x10 ⁻⁹
1-butanol	3.8x10 ⁻¹³	4.1x10 ⁻¹⁰
benzene	5x10 ⁻¹⁷	1.09x10 ⁻¹⁵
p-xylene	3.4x10 ⁻¹⁷	2.02x10 ⁻¹⁵
m-xylene	1.4x10 ⁻¹⁷	1.66x10 ⁻²⁷
o-xylene	8.5x10 ⁻¹⁸	3.92x10 ⁻²⁰

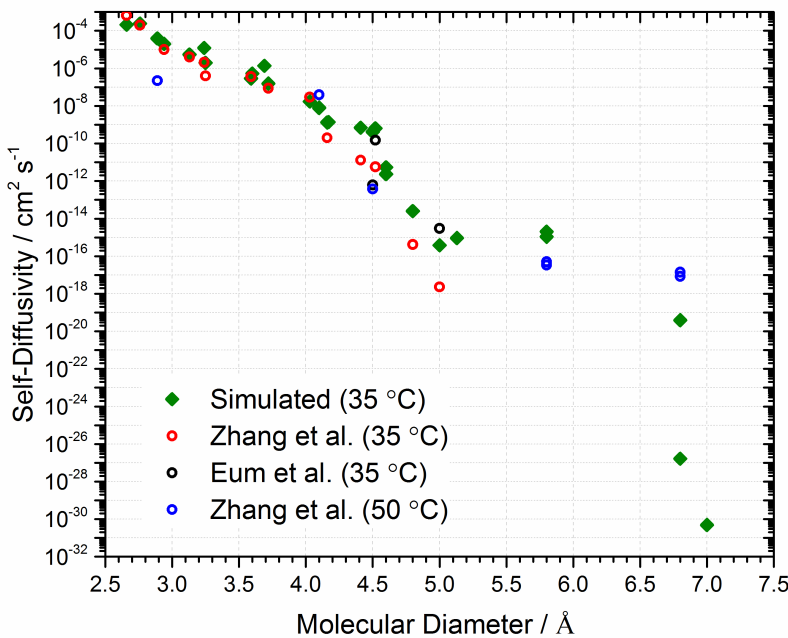


Figure S.27. Comparisons of simulated and experimental self-diffusivities in ZIF-8 at infinite dilution and at the temperatures listed in the legend. The experimental data is taken from Zhang et al.³⁰ (open red circles), Eum et al.³³ (open black circles), and Zhang et al.³² (open blue circles).

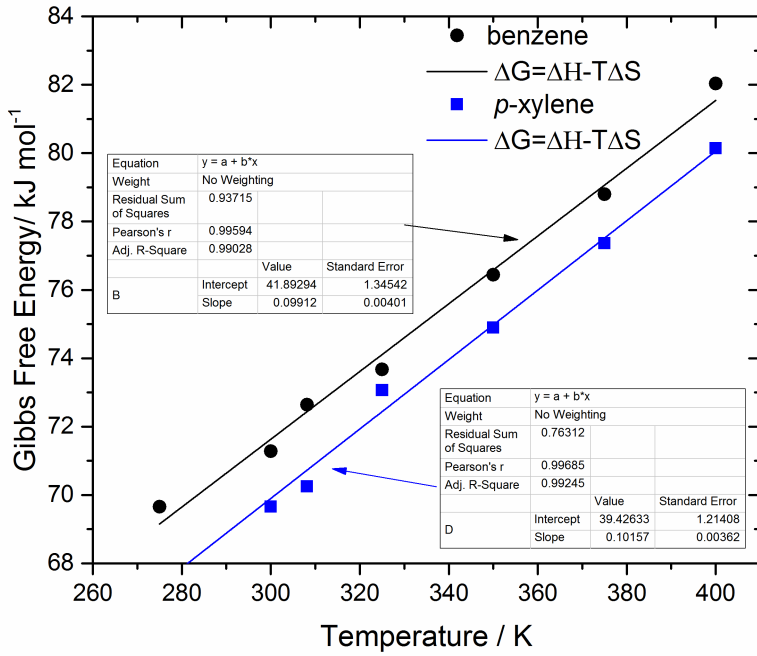


Figure S.28. Gibbs free energy barriers of benzene and p-xylene as a function of temperature. Lines are linear fits to decouple the entropic and enthalpic contributions to diffusion.

Freeman Fitting Parameters

When fitting **Equation 13** in the main manuscript, we use methane as our reference adsorbate where d_{ref} is 3.25 Å and $D_{s,ref}$ is 1.19×10^{-5} , 2.14×10^{-5} , and 1.95×10^{-6} cm² s⁻¹ for SALEM-2, ZIF-90, and ZIF-8 respectively. The fit parameters c' are 0.415, 0.810, and 1.08 Å⁻² with MAEs calculated by

$$\log\left(\frac{D_{s,i}}{D_{s,ref}}\right) \quad (\text{S.1})$$

yielding 0.76, 2.70, and 2.79 for SALEM-2, ZIF-90, and ZIF-8 respectively. The calculation of c' for polymers was performed using

$$c' = \left(\frac{1-a}{RT} \right) c \quad (\text{S.2})$$

with parameters $a=0.64$ and $c=250-2400$ cal mol⁻¹ Å⁻² according to Freeman.³⁴

Linker Swinging in the SALEM-2, ZIF-7, ZIF-8, and ZIF-90

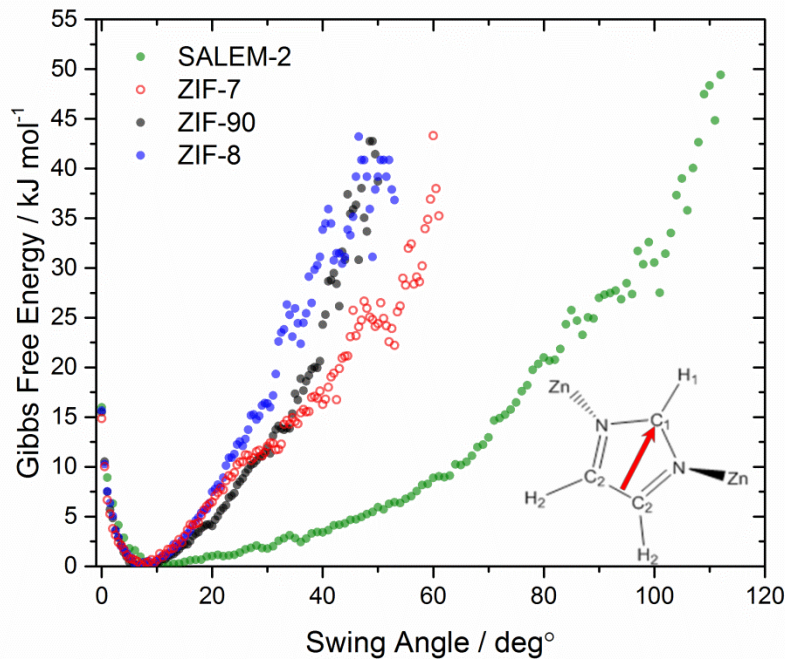
The calculation of window size distributions is not always a clear metric for predicting flexibility of ZIF materials and furthermore requires long molecular dynamics trajectories. We explored measuring the imidazolate swing angle as metric for ranking ZIF flexibility. The linker swing angle is defined by measuring the deviation of an arbitrary vector on the imidazolate ring from its energy minimized position. From the inset in **Figure S.29a**, the vector (red arrow) is defined by the Cartesian coordinates of the C₁ and midpoint of the C₂ atoms. This vector definition can be applied to all ZIF materials. From the periodic BOMD simulations performed at 700 K and 1.01 bar of ZIF-7, ZIF-8, ZIF-90, and SALEM-2, we measured the linker swing angle probability distributions and reported the free energy barriers in **Figure S.29a** as calculated by the following expression

$$G(\theta) = -kT \ln(P(\theta)) \quad (\text{S.3})$$

where G is the Gibbs free energy, k is the ideal gas constant, T is temperature, and P is the probability of observing a swing angle of θ . We find that to access a swing angle of 40°, the free energy barriers rank as follows: SALEM-2 (3.4 kJ mol⁻¹), ZIF-7 (16.3 kJ mol⁻¹), ZIF-90 (24.3 kJ mol⁻¹), and ZIF-8 (33.8 kJ mol⁻¹). This observation directly correlates with the diffusivity results reported in **Figure 10** and the calculation does not require the simulation of long trajectories. Short BOMD simulations (~4 ps) can be used to predict this flexibility behavior.

One interesting feature from the free energy curves is that mean swing angle is not centered at zero. To explain this behavior, we also calculated the linker swing angle in SALEM-2 from BOMD simulations at 100, 200, 300, 500, and 700 K and 1.01 bar as reported in **Figure S.29b**. We find that the average linker swing angle is not constant with temperature (inset of **Figure S.29b**). This observation suggests that the swinging motion of the imidazolate linkers in these materials is highly anharmonic.

(a)



(b)

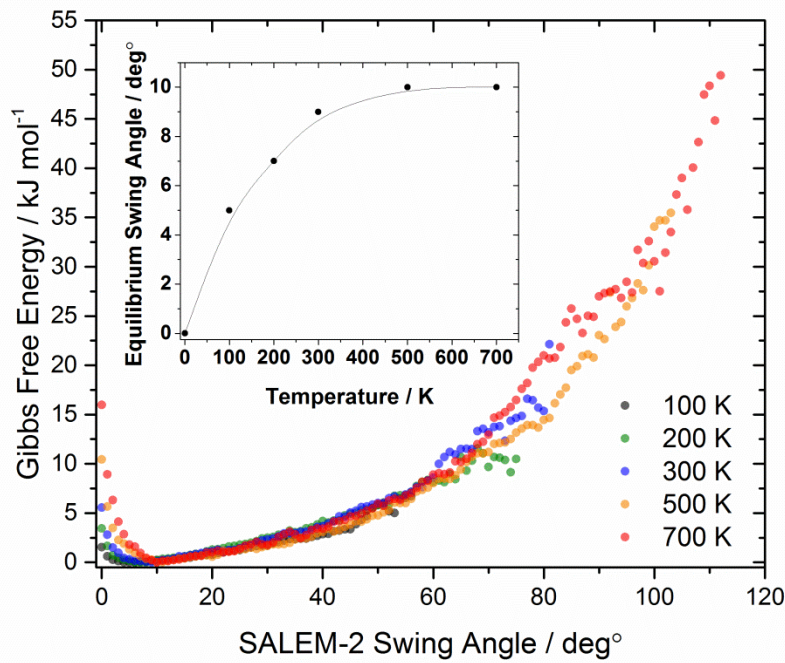


Figure S29. (a) Swing angle of SALEM-2, ZIF-7, ZIF-90, and ZIF-8 as measured from periodic BOMD simulations at 700 K and 1.01 bar. The inset image illustrates that definition of the vector used to quantifying linker swinging. (b) Swing angle of SALEM-2 as a function of temperature as measured from periodic BOMD simulations at 1.01 bar. The inset details the mean swing angle as a function of temperature.

Focused Discussion of Diffusion in ZIF-7

Figure S.30 shows the simulated XRD patterns for the three metastable phases of ZIF-7.

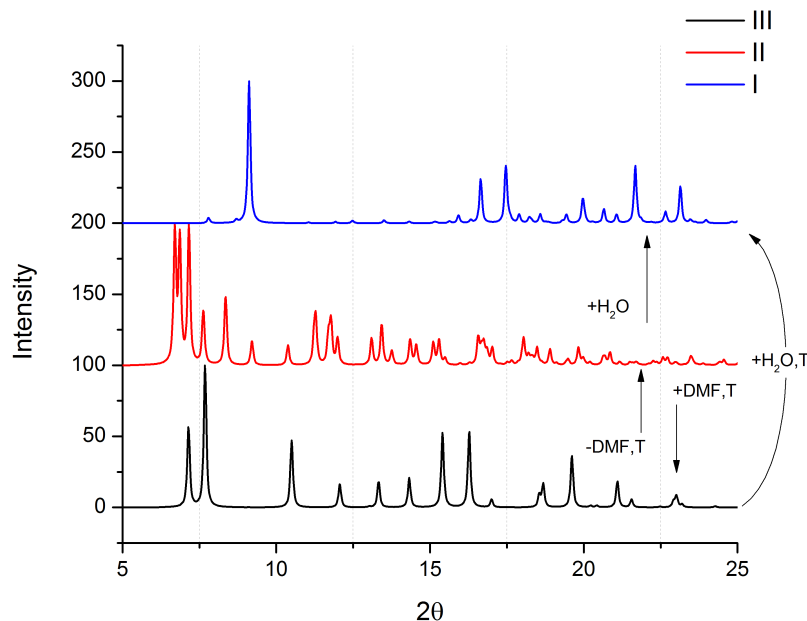


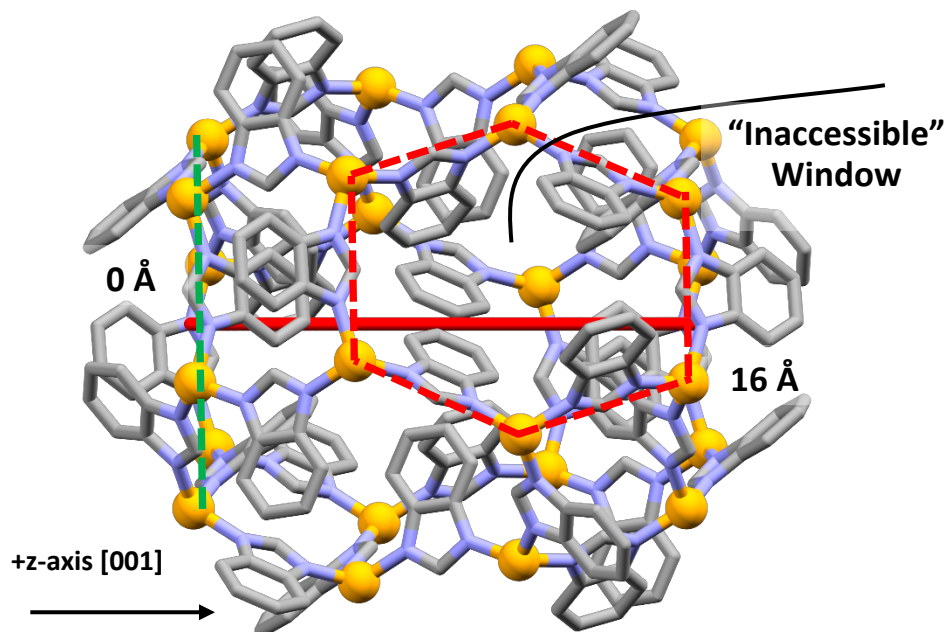
Figure S.30. Simulated XRD patterns for the three stable metaphases of ZIF-7 as reported by Zhao et al. along with routes of formation depending on loading/activation, temperature (T), and degradation.³⁵

Inspection of ZIF-7-I reveals what we will call minor cages formed by the six benzimidazolate linkers surrounding the 6MR window, the plane of which is shown by the dashed green line in **Figure S.31a**. We originally proposed that self-diffusion proceeds in ZIF-7 as a hopping process controlled by the rate from the minor cages into the center of the major sodalite cage. This is supported by the calculated Gibbs free energy barriers from minor cage to minor cage as shown in **Figure S.31b**. The distance from the center of one minor cage to another is 15.95 Å. From Zeo++ calculations on the rigid structure, the 6MR window outlined in red dashed lines in **Figure S.31a** is hypothesized to be inaccessible to adsorbates larger than 1.8 Å in diameter. Zhao et al. previously denoted the minor cage as cavity A and the inaccessible 6MR window as cavity B.³⁶ They showed using high-resolution neutron powder diffraction that cavity B opens upon adsorption of CO₂ at high loadings, and therefore we assume that this gate-opening is not observed at near infinite dilution. Even if motion of the BzIm linkers allows diffusion through cavity B, we

originally hypothesized that diffusion is dominated by hopping through cavity A, which has the larger PLD.

When calculating a diffusivity with **Equation 10** in the main manuscript, we assume the number of windows is 2 and the diffusion occurs in the z-direction (i.e. the dimensionality is 1). The integral of the free energy curve used to calculate the hopping rate in **Equation 10** is performed over the minor cage microstate. Transmission coefficients were calculated along the [001] vector for trajectories leaving from the minor cage at the point designated 0 Å as in **Figure S.31a**. To validate this approach, we have also calculated the self-diffusivities as well as the diagonal components of the diffusivity tensor (D_{xx}, D_{yy}, D_{zz}) at a loading of 3 molecules per unit cell and 308 K using conventional NPT-MD in combination with the Einstein relation³⁷. All the predicted self-diffusivities from both dynamically corrected TST and conventional NPT-MD are reported in **Table S.31**.

(a)



(b)

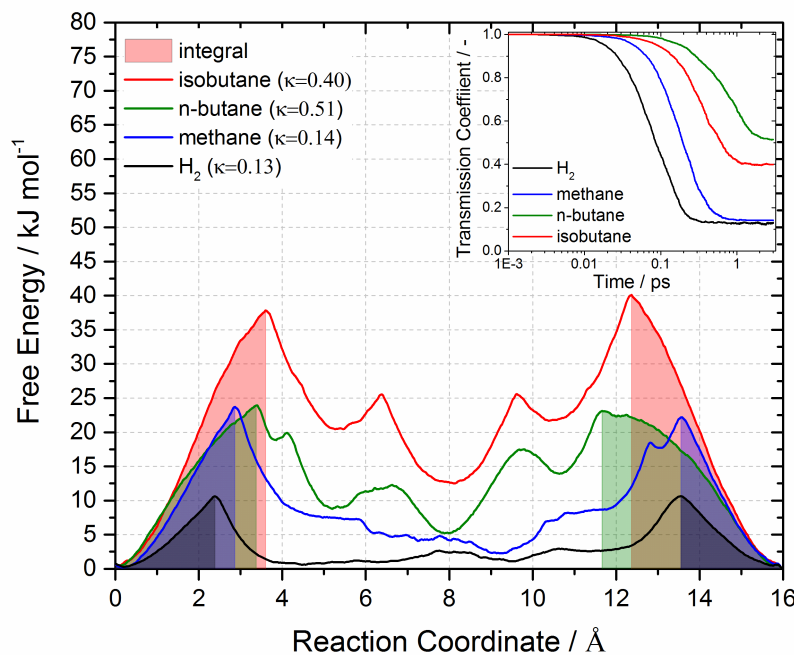


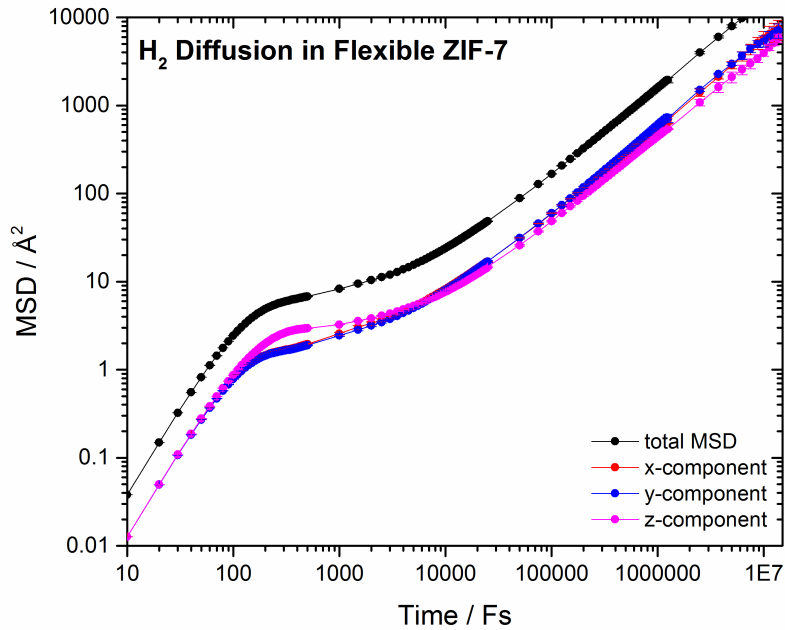
Figure S.31. Analysis of diffusion in ZIF-7-I phase with (a) a singular truncated octahedron cage viewed perpendicular to (010) along with the one-dimensional reaction coordinate (solid red line). The plane of the minor cage is indicated by the dashed green line and the inaccessible window is indicated by the dashed red lines. (b) Gibbs free energy curves at 308 K and 1.01 bar as a function of reaction coordinate. The shaded regions represent the integral used to calculate the TST hopping rate. The inset show the transmission coefficient curves for H_2 , methane, n-butane, and isobutane.

Table S.31. Summary of predicted diffusivities in the ZIF-7-I phase using both conventional NPT-MD and dynamically corrected TST at 308 K and 1.01 bar. Mean squared displacement plots for H₂, CH₄, and n-butane are reported in **Figures S.32a, S.33a, and S.33b**.

Adsorbate (Molecular Diameter / Å)	D_{self}^{MD} [cm ² s ⁻¹]	$D_{self,xx}^{MD}$ [cm ² s ⁻¹]	$D_{self,yy}^{MD}$ [cm ² s ⁻¹]	$D_{self,zz}^{MD}$ [cm ² s ⁻¹]	$D_{self,zz}^{TST}$ [cm ² s ⁻¹]
H ₂ (2.76)	(2.6±0.3)×10 ⁻⁵	(2.5±0.7)×10 ⁻⁵	(2.9±0.5)×10 ⁻⁵	(2.4±0.8)×10 ⁻⁵	1.39×10 ⁻⁴
N ₂ (3.13)	(1.5±0.2)×10 ⁻⁶	(1.7±0.7)×10 ⁻⁶	(2.1±0.4)×10 ⁻⁶	(6.7±0.6)×10 ⁻⁷	-
CO ₂ (3.24)	(4.6±1.4)×10 ⁻⁷	(4.6±3.1)×10 ⁻⁷	(7.0±1.5)×10 ⁻⁷	(2.3±0.8)×10 ⁻⁷	-
CH ₄ (3.25)	(1.8±0.4)×10 ⁻⁶	(1.6±0.9)×10 ⁻⁶	(2.7±1.2)×10 ⁻⁶	(9.9±0.5)×10 ⁻⁷	4.74×10 ⁻⁷
n-butane (4.52)	(1.1±0.1)×10 ⁻⁶	(1.5±0.6)×10 ⁻⁶	(1.3±0.3)×10 ⁻⁶	(4.9±1.6)×10 ⁻⁷	9.66×10 ⁻⁷
isobutane (5.0)	-	-	-	-	1.48×10 ⁻⁹

Figure S.32 shows MSDs for H₂ in flexible and rigid ZIF-7-I at 308 K. **Figure S.33** shows the MSDs for methane and n-butane in flexible ZIF-7-I at 308 K. **Figures S.34 and S.35** show trajectories taken by H₂ and CO₂ molecules respectively in flexible ZIF-7-I at 308 K.

(a)



(b)

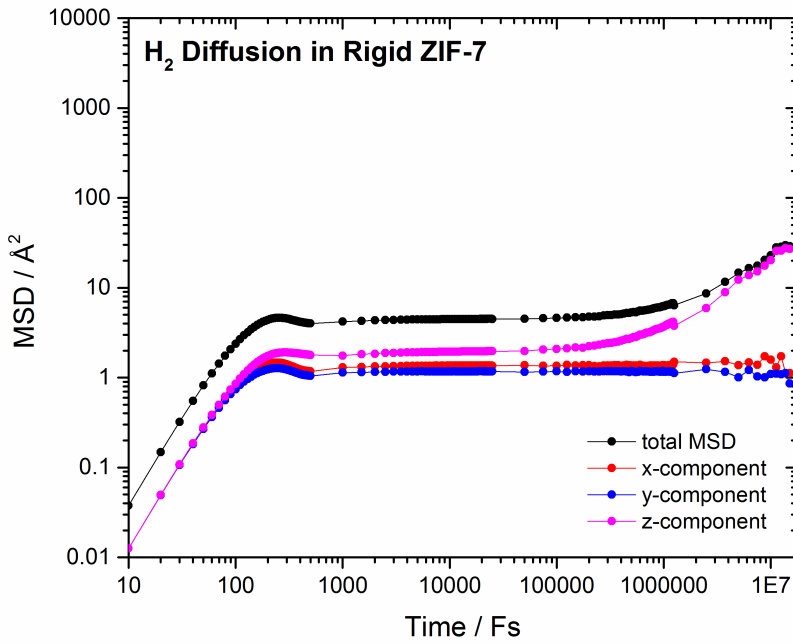
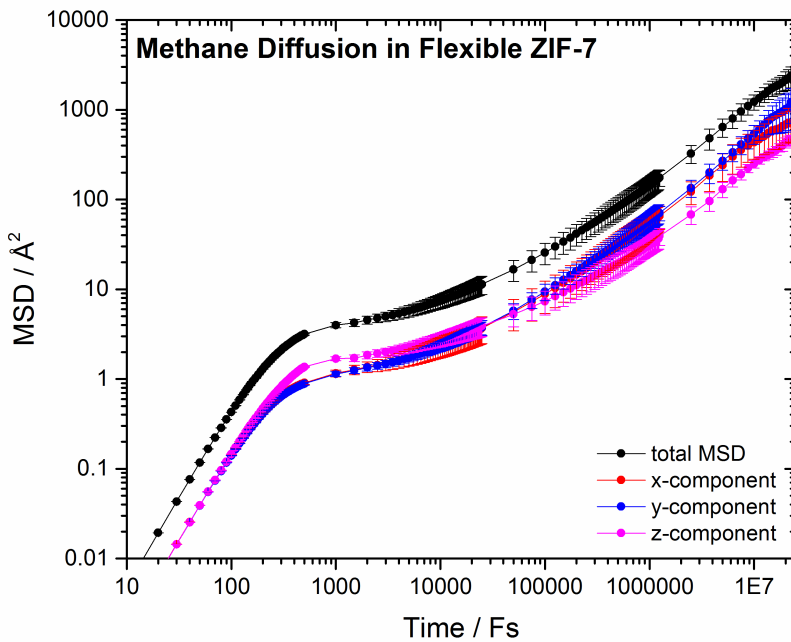


Figure S.32. Total and directional MSDs for H₂ diffusion in (a) flexible and (b) rigid ZIF-7-I at a loading of three adsorbates per unit cell, 1.01 bar, and 308 K.

(a)



(b)

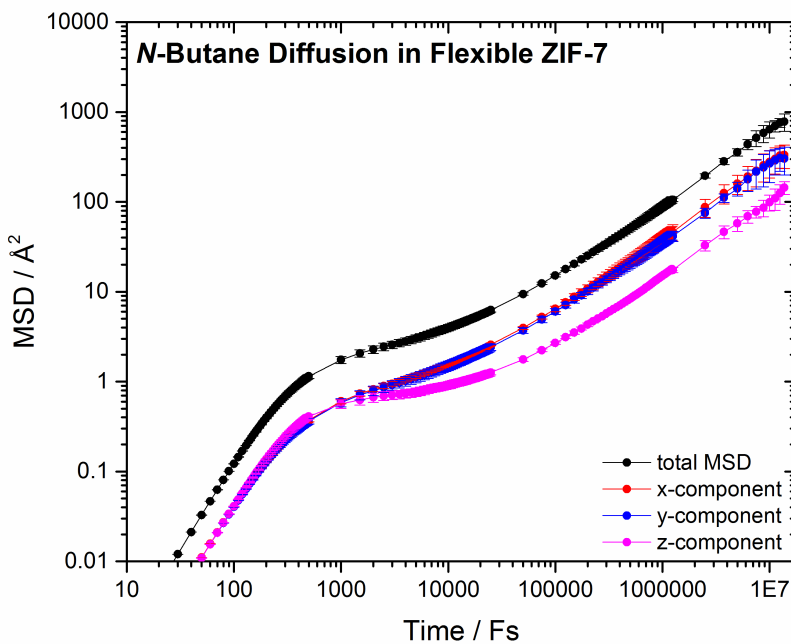


Figure S.33. MSDs for (a) methane and (b) n-butane in flexible ZIF-7-I at a loading of three adsorbates per unit cell, 1.01 bar, and 308 K.

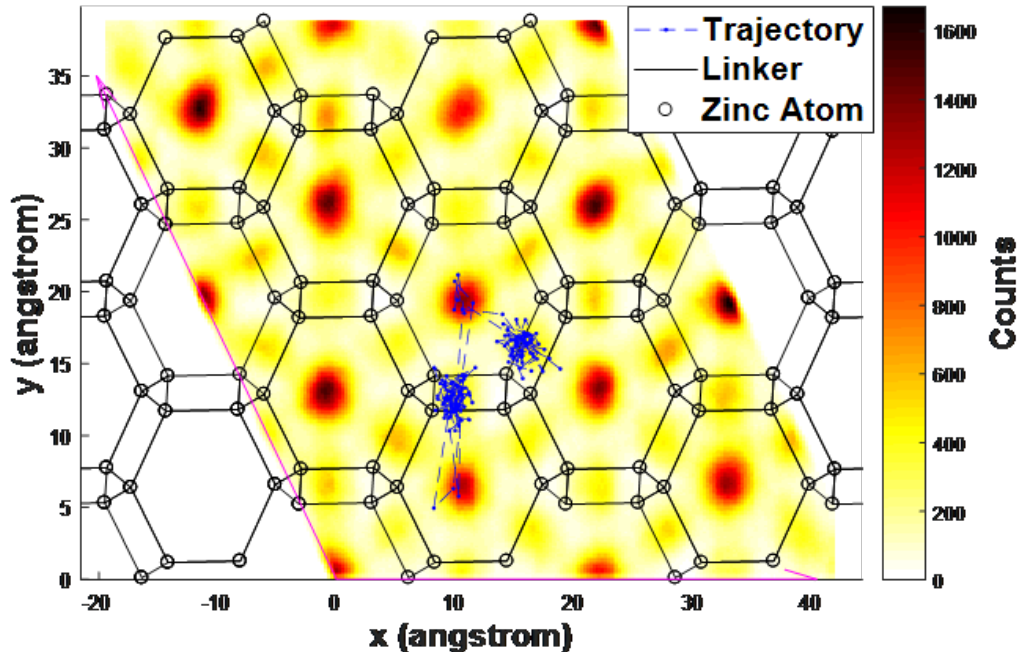


Figure S.34. XY projection of the H₂ trajectories in the flexible ZIF-7-I structure. The XY-plane of the expanded ZIF-7 unit cell was divided into a 250 by 250 rectangular grid. Each grid point was sampled every 500 fs over a 10 ns trajectory, and the intensity of each sampled grid point was increased by the number of H₂ molecules whose XY centroid was within 0.5 Å (calculated using Euclidean Norm). The blue line shows the XY trajectory of a single H₂ sampled every 5 ps over a 750 ps trajectory. The Zn-linker overlay (black lines) on the graph is taken from the empty expanded rigid structure.

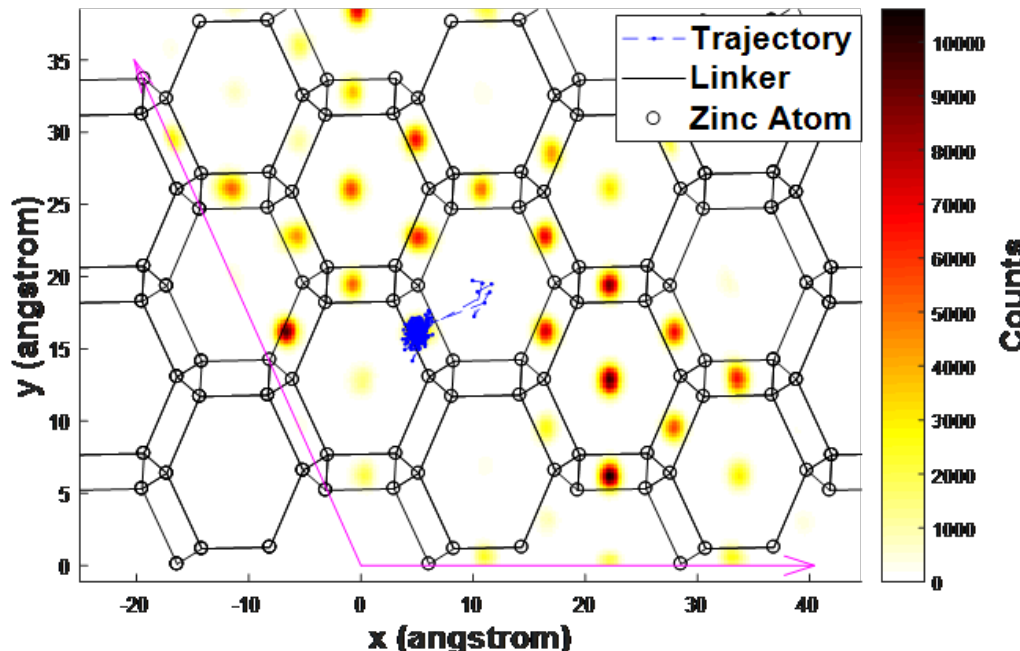


Figure S.35. XY projection of the CO₂ trajectories in the flexible ZIF-7-I structure. The blue line shows the XY trajectory of a single CO₂ sampled every 5 ps over a 1000 ps trajectory. All other plot features are the same as shown in Figure S.33.

Figure S.36 shows the accessible volume fraction as a function of hydrocarbon loading in ZIF-7 at 308 K. Accessible volume fractions were calculated using Zeo++ in snapshots from an NPT-MD simulation in LAMMPS. The NPT-MD simulation was equilibrated for 1 ns and a snapshot were recorded every 5000 fs over a 5 ns production simulation (i.e. 1000 snapshots). Each simulation had a loading of three molecules per unit cell and the adsorbates were removed from the snapshots before the accessible volume calculation.

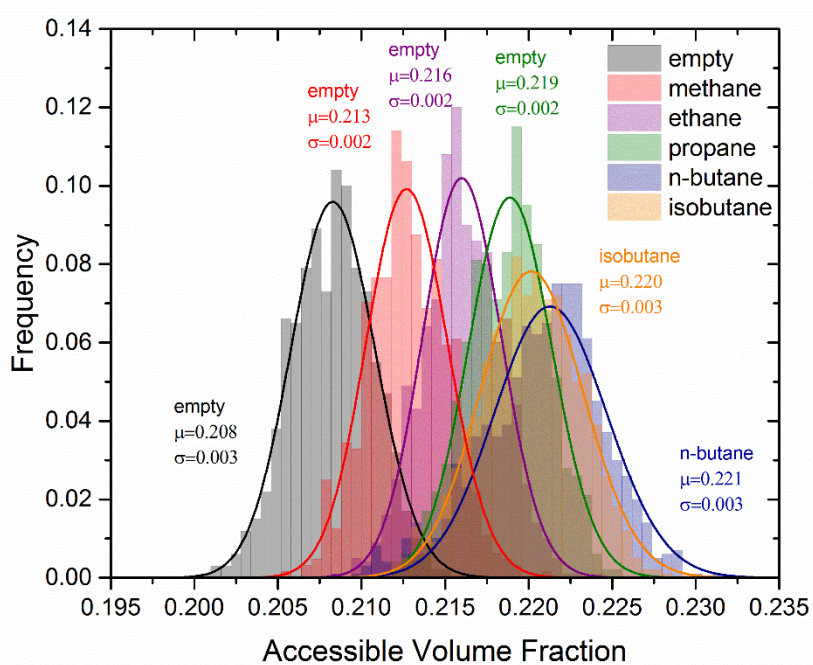


Figure S.36. Accessible volume fraction distributions of ZIF-7 at 308 K and under various hydrocarbon loading conditions. Lognormal distributions are shown by the solid lines and the mean (μ) and standard deviation (σ) are reported as text in the figure.

Thermodynamic Stability of Im and mIm ZIF Polymorphs

ZIFs exhibit polymorphism³⁸ and there are abundant experimental and computational studies examining their thermodynamic stability³⁹⁻⁴⁰. Methods such as the osmotic adsorbed solution theory (OFAST)⁴¹ and thermodynamic cycles examining relative stability⁴² require the relative configurational potential energies of different polymorphs⁴³. Studying extended defects in ZIF defects and predicting how these defects influence diffusion requires the use of a FF due to large system sizes.⁴⁴ For these reasons, it is useful to have a force field that predicts the correct thermodynamic stability trends. We therefore calculated the relative configurational potential energy ranking of the originally reported twenty-seven Im⁴⁰ and twenty-five mIm³⁹ ZIF polymorphs with respect to the dense *zni* polymorph using PBE-D2 as well as the AMBER and intraZIF FFs, as shown in **Figure S.37**. We used the full set of polymorphs reported by Baburin et al. for each linker. Our DFT calculations predict the *zni* and the *dia* topology to be the most stable polymorph of the Im and mIm ZIF polymorphs, respectively, in agreement with prior computational studies on the Im ZIF polymorphs.^{39-40, 45} The relative energy rankings using PBE-D3(BJ) are similar to those using PBE-D2, as shown in **Tables S.18** and **S.19**.

The AMBER-FF performs considerably better than the intraZIF-FF at predicting the PBE-D2/PBE-D3(BJ) relative energy differences, but neither give accurate thermodynamic stability rankings. This is not terribly surprising given both FFs are parameterized to reproduce the tetrahedral coordination environment of the Zn (see **Figure S.20** for representative coordination environments). **Figure S.19** shows that the average N-Zn-N angle is ~109.4° for all the Im polymorphs. The maximum and minimum angles, however, deviate greatly for some structures. For example, the *uoc* polymorph has minimum and maximum N-Zn-N angles of 91° and 162° respectively. The AMBER-FF correctly predicts that Im-*zni* and mIm-*dia* polymorphs are lowest in energy for both sets. However, it incorrectly predicts that eight other mIm polymorphs, besides the mIm-*dia* polymorph, are lower in energy than the mIm-*zni* polymorph as seen in **Figure S.37**. The intraZIF-FF predicts that the mIm-*dia* polymorph is 11.6 kJ/mol/Zn higher in energy than the mIm-*zni* polymorph, but correctly predicts that all the other mIm polymorphs are higher in energy than the mIm-*zni* polymorph. The intraZIF-FF could be improved by either including the van der Waals interactions in the fitting procedure, tuning the empirical Debye interactions, or modeling the near square planar and tetrahedral coordination environments with separate harmonic

potentials. The relative energy difference between different polymorphs does not have an impact on diffusion calculations. The accuracy of diffusivity prediction usually depends on framework dynamics, adsorbate–framework interactions, and pore size.

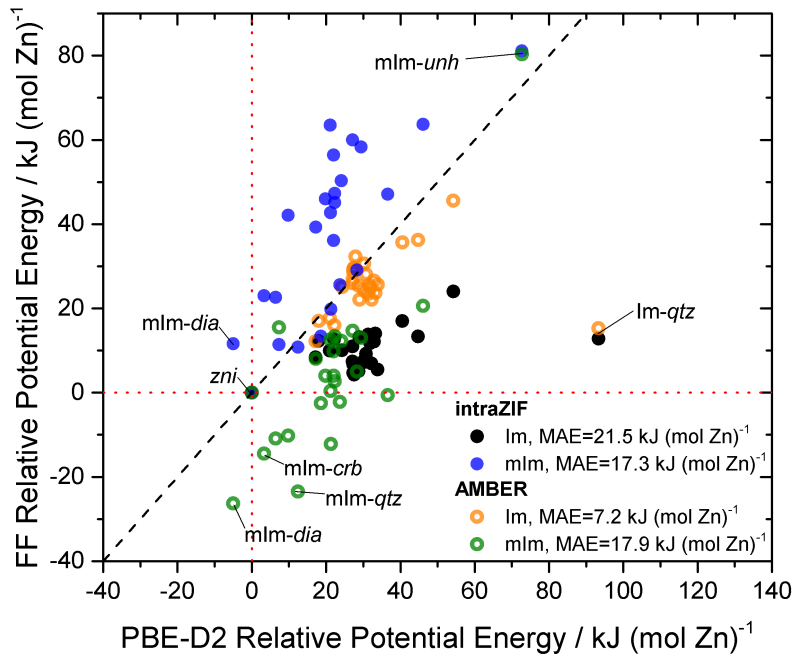


Figure S.37. Relative energy rankings of the hypothetical **(a)** imidazolate (black/orange) and **(b)** 2-methylimidazolate (blue/green) polymorphs for PBE-D2, the AMBER-FF (open circles), and the intraZIF-FF (closed circles). The red dashed lines highlight polymorphs that are predicted to be lower in energy than the *zni* polymorphs.

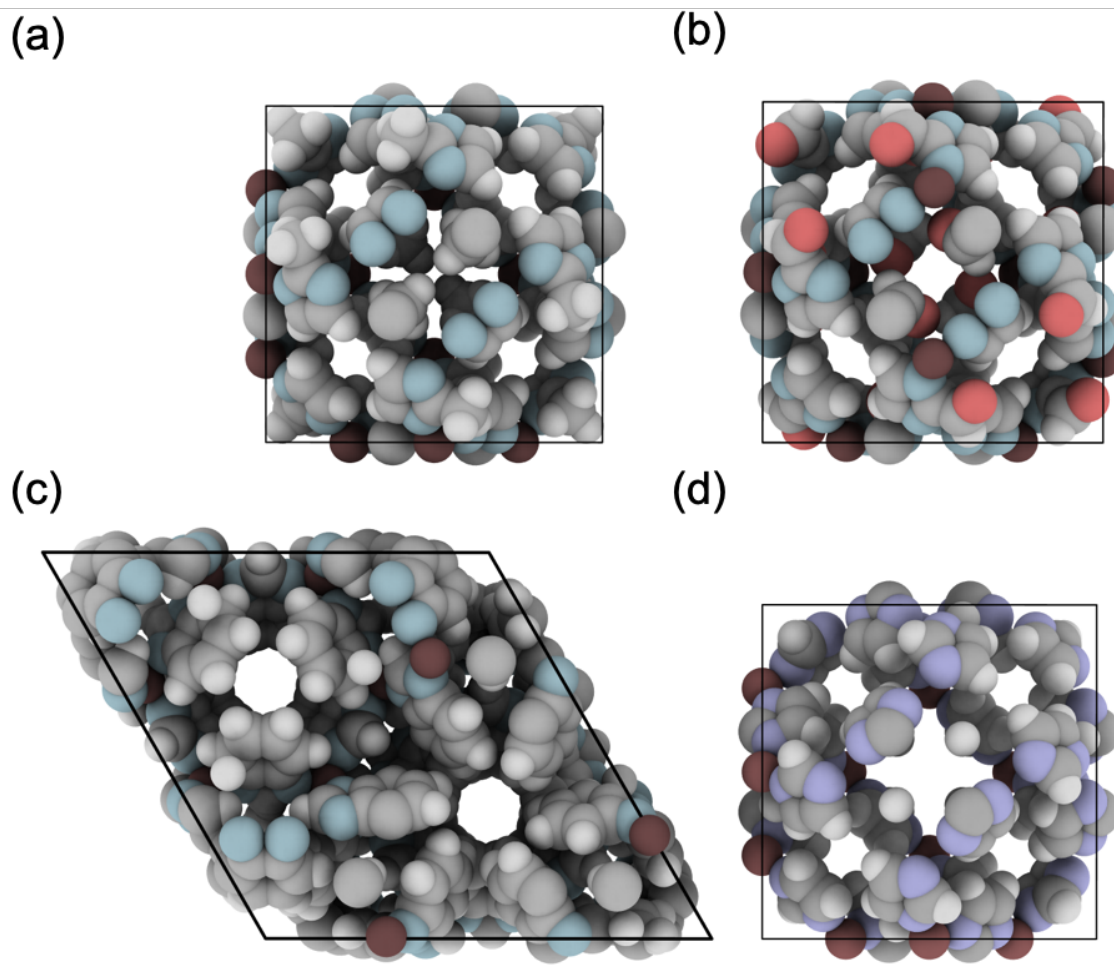


Figure S.38. Unit cell of (a) ZIF-8, (b) ZIF-90, (c) ZIF-7, and (d) SALEM-2 structures.

Supporting Information References

1. Zheng, B.; Sant, M.; Demontis, P.; Suffritti, G. B., Force Field for Molecular Dynamics Computations in Flexible ZIF-8 Framework. *J. Phys. Chem. C* **2012**, *116*, 933-938.
2. Zhang, L.; Hu, Z.; Jiang, J., Sorption-Induced Structural Transition of Zeolitic Imidazolate Framework-8: A Hybrid Molecular Simulation Study. *J. Am. Chem. Soc.* **2013**, *135*, 3722-3728.
3. Manz, T. A.; Sholl, D. S., Chemically Meaningful Atomic Charges That Reproduce the Electrostatic Potential in Periodic and Nonperiodic Materials. *J. Chem. Theory Comput.* **2010**, *6*, 2455-2468.
4. Manz, T. A.; Sholl, D. S., Improved Atoms-in-Molecule Charge Partitioning Functional for Simultaneously Reproducing the Electrostatic Potential and Chemical States in Periodic and Nonperiodic Materials. *J. Chem. Theory Comput.* **2012**, *8*, 2844-2867.
5. Verploegh, R. J.; Nair, S.; Sholl, D. S., Temperature and Loading-Dependent Diffusion of Light Hydrocarbons in ZIF-8 as Predicted through Fully Flexible Molecular Simulations. *J. Am. Chem. Soc.* **2015**, *137*, 15760-15771.
6. Fang, H.; Demir, H.; Kamakoti, P.; Sholl, D. S., Recent Developments in First-Principles Force Fields for Molecules in Nanoporous Materials. *J. Mater. Chem. A* **2014**, *2*, 274-291.
7. Cornell, W. D.; Cieplak, P.; Bayly, C. I.; Gould, I. R.; Merz, K. M.; Ferguson, D. M.; Spellmeyer, D. C.; Fox, T.; Caldwell, J. W.; Kollman, P. A., A Second Generation Force Field for the Simulation of Proteins, Nucleic Acids, and Organic Molecules. *J. Am. Chem. Soc.* **1995**, *117*, 5179-5197.
8. Allinger, N. L.; Yuh, Y. H.; Lii, J. H., Molecular Mechanics. The MM3 Force Field for Hydrocarbons. 1. *J. Am. Chem. Soc.* **1989**, *111*, 8551-8566.
9. Allinger, N. L.; Zhou, X.; Bergsma, J., Molecular Mechanics Parameters. *J. Mol. Struct.: THEOCHEM* **1994**, *312*, 69-83.
10. Willemse, T. F.; Rycroft, C. H.; Kazi, M.; Meza, J. C.; Haranczyk, M., Algorithms and Tools for High-Throughput Geometry-Based Analysis of Crystalline Porous Materials. *Microporous Mesoporous Mater.* **2012**, *149*, 134-141.
11. Talu, O.; Myers, A. L., Molecular Simulation of Adsorption: Gibbs Dividing Surface and Comparison with Experiment. *AIChE J.* **2001**, *47*, 1160-1168.
12. Camp, J. S.; Sholl, D. S., Transition State Theory Methods to Measure Diffusion in Flexible Nanoporous Materials: Application to a Porous Organic Cage Crystal. *J. Phys. Chem. C* **2016**, *120*, 1110-1120.
13. Clark, L. A.; Gupta, A.; Snurr, R. Q., *J. Phys. Chem. B* **1998**, *102*, 6720-6731.
14. Brand, S. K.; Colón, Y. J.; Getman, R. B.; Snurr, R. Q., Design Strategies for Metal Alkoxide Functionalized Metal–Organic Frameworks for Ambient Temperature Hydrogen Storage. *Microporous Mesoporous Mater.* **2013**, *171*, 103-109.
15. Zhang, L.; Siepmann, J. I., Direct Calculation of Henry's Law Constants from Gibbs Ensemble Monte Carlo Simulations: Nitrogen, Oxygen, Carbon Dioxide and Methane in Ethanol. *Theor. Chem. Acc.* **2006**, *115*, 391-397.
16. Potoff, J. J.; Siepmann, J. I., Vapor–Liquid Equilibria of Mixtures Containing Alkanes, Carbon Dioxide, and Nitrogen. *AIChE J.* **2001**, *47*, 1676-1682.
17. Harris, J. G.; Yung, K. H., Carbon Dioxide's Liquid-Vapor Coexistence Curve and Critical Properties as Predicted by a Simple Molecular Model. *J. Phys. Chem.* **1995**, *99*, 12021-12024.
18. Chen, B.; Potoff, J. J.; Siepmann, J. I., Monte Carlo Calculations for Alcohols and Their Mixtures with Alkanes. Transferable Potentials for Phase Equilibria. 5. United-Atom Description of Primary, Secondary, and Tertiary Alcohols. *J. Phys. Chem. B* **2001**, *105*, 3093-3104.
19. Martin, M. G.; Siepmann, J. I., Transferable Potentials for Phase Equilibria. 1. United-Atom Description of N-Alkanes. *J. Phys. Chem. B* **1998**, *102*, 2569-2577.
20. Wick, C. D.; Martin, M. G.; Siepmann, J. I., Transferable Potentials for Phase Equilibria. 4. United-Atom Description of Linear and Branched Alkenes and Alkylbenzenes. *J. Phys. Chem. B* **2000**, *104*, 8008-8016.
21. Stubbs, J. M.; Potoff, J. J.; Siepmann, J. I., Transferable Potentials for Phase Equilibria. 6. United-Atom Description for Ethers, Glycols, Ketones, and Aldehydes. *J. Phys. Chem. B* **2004**, *108*, 17596-17605.
22. Dubbeldam, D.; Calero, S.; Vlugt, T. J. H.; Krishna, R.; Maesen, T. L. M.; Smit, B., United Atom Force Field for Alkanes in Nanoporous Materials. *J. Phys. Chem. B* **2004**, *108*, 12301-12313.
23. Jorgensen, W. L.; Laird, E. R.; Nguyen, T. B.; Tirado-Rives, J., Monte Carlo Simulations of Pure Liquid Substituted Benzenes with Opls Potential Functions. *J. Comput. Chem.* **1993**, *14*, 206-215.
24. Castillo, J. M.; Vlugt, T. J. H.; Calero, S., Molecular Simulation Study on the Separation of Xylene Isomers in Mil-47 Metal–Organic Frameworks. *J. Phys. Chem. C* **2009**, *113*, 20869-20874.
25. Berendsen, H. J. C.; Grigera, J. R.; Straatsma, T. P., The Missing Term in Effective Pair Potentials. *J. Phys. Chem.* **1987**, *91*, 6269-6271.

26. Orsi, M., Comparative Assessment of the Elba Coarse-Grained Model for Water. *Mol. Phys.* **2014**, *112*, 1566-1576.
27. Chalaris, M.; Samios, J., Systematic Molecular Dynamics Studies of Liquid N, N-Dimethylformamide Using Optimized Rigid Force Fields: Investigation of the Thermodynamic, Structural, Transport and Dynamic Properties. *J. Chem. Phys.* **2000**, *112*, 8581-8594.
28. Rai, N.; Siepmann, J. I., Transferable Potentials for Phase Equilibria. 9. Explicit Hydrogen Description of Benzene and Five-Membered and Six-Membered Heterocyclic Aromatic Compounds. *J. Phys. Chem. B* **2007**, *111*, 10790-10799.
29. Sanjeewa, R.; Weerasinghe, S., Development of a Molecular Mechanics Force Field for Caffeine to Investigate the Interactions of Caffeine in Different Solvent Media. *J. Mol. Struct.: THEOCHEM* **2010**, *944*, 116-123.
30. Zhang, C.; Lively, R. P.; Zhang, K.; Johnson, J. R.; Karvan, O.; Koros, W. J., Unexpected Molecular Sieving Properties of Zeolitic Imidazolate Framework-8. *J. Phys. Chem. Lett.* **2012**, *3*, 2130-2134.
31. Wu, H.; Gong, Q.; Olson, D. H.; Li, J., Commensurate Adsorption of Hydrocarbons and Alcohols in Microporous Metal Organic Frameworks. *Chem. Rev.* **2012**, *112*, 836-868.
32. Zhang, K.; Lively, R. P.; Zhang, C.; Chance, R. R.; Koros, W. J.; Sholl, D. S.; Nair, S., Exploring the Framework Hydrophobicity and Flexibility of ZIF-8: From Biofuel Recovery to Hydrocarbon Separations. *J. Phys. Chem. Lett.* **2013**, *4*, 3618-3622.
33. Eum, K., et al., Highly Tunable Molecular Sieving and Adsorption Properties of Mixed-Linker Zeolitic Imidazolate Frameworks. *J. Am. Chem. Soc.* **2015**, *137*, 4191-4197.
34. Freeman, B. D., Basis of Permeability/Selectivity Tradeoff Relations in Polymeric Gas Separation Membranes. *Macromolecules* **1999**, *32*, 375-380.
35. Zhao, P.; Lampronti, G. I.; Lloyd, G. O.; Wharmby, M. T.; Facq, S.; Cheetham, A. K.; Redfern, S. A. T., Phase Transitions in Zeolitic Imidazolate Framework 7: The Importance of Framework Flexibility and Guest-Induced Instability. *Chem. Mater.* **2014**, *26*, 1767-1769.
36. Zhao, P.; Lampronti, G. I.; Lloyd, G. O.; Suard, E.; Redfern, S. A. T., Direct Visualisation of Carbon Dioxide Adsorption in Gate-Opening Zeolitic Imidazolate Framework ZIF-7. *J. Mater. Chem. A* **2014**, *2*, 620-623.
37. Skouidas, A. I.; Sholl, D. S., Self-Diffusion and Transport Diffusion of Light Gases in Metal-Organic Framework Materials Assessed Using Molecular Dynamics Simulations. *J. Phys. Chem. B* **2005**, *109*, 15760-15768.
38. Park, K. S.; Ni, Z.; Côté, A. P.; Choi, J. Y.; Huang, R.; Uribe-Romo, F. J.; Chae, H. K.; O'Keeffe, M.; Yaghi, O. M., Exceptional Chemical and Thermal Stability of Zeolitic Imidazolate Frameworks. *Proc. Natl. Acad. Sci. U. S. A.* **2006**, *103*, 10186-10191.
39. Baburin, I. A.; Leoni, S., The Energy Landscapes of Zeolitic Imidazolate Frameworks (ZIFs): Towards Quantifying the Presence of Substituents on the Imidazole Ring. *J. Mater. Chem.* **2012**, *22*, 10152-10154.
40. Baburin, I. A.; Leoni, S.; Seifert, G., Enumeration of Not-yet-Synthesized Zeolitic Zinc Imidazolate MOF Networks: A Topological and Dft Approach. *J. Phys. Chem. B* **2008**, *112*, 9437-9443.
41. Coudert, F.-X.; Jeffroy, M.; Fuchs, A. H.; Boutin, A.; Mellot-Draznieks, C., Thermodynamics of Guest-Induced Structural Transitions in Hybrid Organic-Inorganic Frameworks. *J. Am. Chem. Soc.* **2008**, *130*, 14294-14302.
42. Gee, J. A.; Sholl, D. S., Characterization of the Thermodynamic Stability of Solvated Metal-Organic Framework Polymorphs Using Molecular Simulations. *J. Phys. Chem. C* **2013**, *117*, 20636-20642.
43. Du, Y.; Wooler, B.; Nines, M.; Kortunov, P.; Paur, C. S.; Zengel, J.; Weston, S. C.; Ravikovich, P. I., New High- and Low-Temperature Phase Changes of ZIF-7: Elucidation and Prediction of the Thermodynamics of Transitions. *J. Am. Chem. Soc.* **2015**, *137*, 13603-13611.
44. Han, R.; Sholl, D. S., Computational Model and Characterization of Stacking Faults in ZIF-8 Polymorphs. *J. Phys. Chem. C* **2016**, *120*, 27380-27388.
45. Galvelis, R.; Slater, B.; Cheetham, A. K.; Mellot-Draznieks, C., Comparison of the Relative Stability of Zinc and Lithium-Boron Zeolitic Imidazolate Frameworks. *Cryst. Eng.* **2012**, *14*, 374-378.